Soft Templating and Disorder in an Applied 1D Cobalt Coordination Polymer Electrocatalyst

Triana, Carlos A ; Moré, René ; Bloomfield, Aaron J ; Petrović, Predrag V ; Ferrón, Sara Goberna ; Stanley, George ; Zarić, Snežana D ; Fox, Thomas ; Brothers, Edward N ; Sheehan, Stafford W ; Anastas, Paul T ; Patzke, Greta R

Abstract: Disordered materials with resilient and soft-templated functional units bear the potential to fill the pipeline of robust catalysts for renewable energy storage. However, for novel materials lacking long-range order, the ability to discern local structure with atomic resolution still pushes the boundaries of current analytical and modeling approaches. We introduce a two-pillar strategy to monitor the formation and unravel the structure of the first disordered one-dimensional cobalt coordination polymer catalyst, Co-dppeO2. This target material excels through proven high performance in commercial alkaline electrolyzers and organic transformations. We demonstrate that the key architecture behind this activity is the unconventional embedding of hydrated H2O-Co2(OH)2-OH2 edge-site motifs, nested into a flexible organic matrix of highly oxidized and bridging hydrophobic dppeO2 ligands. Our combination of in situ spectroscopy and computational modeling of X-ray scattering and absorption spectra, backed with complementary experimental techniques, holds the key to understanding the atomic-range structure of important disordered materials.

DOI: https://doi.org/10.1016/j.matt.2019.06.021

Soft Templating and Disorder in an Applied 1D Cobalt Coordination Polymer Electrocatalyst

C. A. Triana,[1] René Moré,[1] Aaron J. Bloomfield,[2,3,*] Predrag V. Petrović,[2] Sara Goberna Ferrón,[4] George Stanley,[5] Snežana D. Zarić,[6,7] Thomas Fox,[1] Edward N. Brothers,[6] Stafford W. Sheehan,[8,*] Paul T. Anastas,[2] and Greta R. Patzke[1,*]

[1] Department of Chemistry, University of Zurich, Winterthurerstrasse 190, CH-8057 Zurich, Switzerland
[2] School of Forestry and Environmental Studies and Yale School of Public Health, Yale University, 225 Prospect Street, New Haven, CT 06520, USA
[3] Department of Chemistry and Biochemistry, Duquesne University, Pittsburgh, PA 15282, USA
[4] European Synchrotron Radiation Facility, 71 avenue des Martyrs, CS 40220, 38043, Grenoble, France
[5] Department of Chemistry, Louisiana State University, Baton Rouge, LA 70803-1804, USA
[6] Science Program, Texas A&M University at Qatar, P.O. Box 23874, Doha, Qatar
[7] Faculty of Chemistry, University of Belgrade, Studentski trg 12-16, Belgrade, Serbia
[8] Catalytic Innovations, 151 Martine St, Fall River, MA 02723, USA
[*] Correspondence: greta.patzke@chem.uzh.ch (G.R.P.), staff@catalytic-innovation.com (S.W.S.), bloomfielda@duq.edu (A.J.B.)

SUMMARY

Disordered materials with resilient and soft-templated functional units bear the potential to fill the pipeline of robust catalysts for renewable energy storage. However, for new material types lacking long-range atomic order, the ability to discern local structure with atomic resolution still pushes the boundaries of current analytical and modeling approaches. To this end, we introduce a complementary two-pillar strategy that both monitors the formation and unravels the structure of the first disordered 1D cobalt coordination polymer catalyst, Co-dppeO_2. This target material excels through proven high performance in commercial alkaline electrolyzers as well as in organic transformations. We demonstrate that the key architecture behind this activity is the unconventional embedding of hydrated {H_2O-$Co_2(OH)_2$-OH_2} edge site motifs, nested into a flexible organic matrix of highly oxidized and bridging hydrophobic dppeO_2 ligands. Our combination of *in situ* spectroscopic methods and computational modeling of experimental X-ray scattering and absorption spectra, backed with complementary experimental techniques, holds the key to understanding the atomic-range structure of important disordered materials.

INTRODUCTION

The growing worldwide need for storable fuels from sustainable energy sources has triggered an intense search for low-cost, robust and flexible catalysts with extended durability under harsh conditions.[1-10] The tremendous influence of disorder on catalytic activity and resilience[11-15] has yet to be fully grasped, and most catalyst development is still based on classic and ordered structure-activity relationships. This contrast between catalytic reality and synthetic strategy is due to considerable difficulties that are still associated with the structural understanding of disordered materials.

Even the analysis of prominent disordered high-performance materials with known catalytic motifs, such as the "CoPi" water oxidation catalyst, "black TiO_2", manganese or vanadium oxide-based oxidation catalysts took time and intense analytical effort.[16-21] While modeling techniques, such as Reverse Monte Carlo (RMC)

simulations, are now available, access to the required high-end analytical techniques, such as X-ray absorption spectroscopy (XAS) or *in situ* high-resolution transmission electron microscopy (HRTEM), is still restricted to beamlines and larger facilities. In short, we are not yet fully equipped to explore an emerging new generation of unconventional and disordered catalysts beyond familiar structural motifs, such as disordered hybrid materials. New methodologies are, therefore, required to fully explore the unconventional potential of these catalyst types.[22-27] Physical chemists are constantly advancing toward bringing XAS equipment and related beamline technologies to benchtop-scales.[28,29] However, even with such instrumentation available, understanding completely new disordered compounds remains challenging *terra incognita,* when no X-ray scattering or detailed nuclear magnetic resonance (NMR) data are at hand.

With our discovery of the unconventional structural features of a disordered high-performance catalyst, we demonstrate analytical concepts that extend beyond empirical performance characterizations. Our representative target material, referred to as Co-dppeO_2, was selected due to its proven and leading performance in oxidation catalysis.[30] First and foremost, it shows high performance as a water oxidation catalyst, outperforming electrodeposited amorphous cobalt oxide (CoO_x) in both clean and contaminated water sources.[31] Co-dppeO_2 demonstrates operational stability on stainless steel electrodes in alkaline electrolyzers for over 60 days without performance reduction.[30] Consequently, facile decagram-scale synthesis of Co-dppeO_2 and its simple incorporation into coatings has furthered its commercial application.[31] Furthermore, Co-dppeO_2 displays cutting-edge multifunctional properties for the electrocatalytic upgrading of organic feedstock when compared to conventional cobalt oxide-based catalysts.[32,33]

Notably, this material emerged from an unconventional crossover synthetic screening strategy of organic ligands for highest catalytic activity in a synthetic system starting from dicobalt octacarbonyl $Co_2(CO)_8$.[31] However, the strongly disordered nature of Co-dppeO_2, i.e. its complete lack of long-range order, forestalled all analytical options to elucidate the underlying structural features with conventional approaches.

Therefore, we developed a state-of-the-art and generally applicable approach based on two complementary pillars, namely *in situ* formation monitoring of Co-dppeO_2 together with computational modeling of X-ray scattering and absorption spectra. To this end, we applied a combination of *in situ* infrared spectroscopy and Density Functional Theory (DFT) to monitor and determine the structure of synthetic intermediate species towards formation of the active site. The structure of the final purified Co-dppeO_2 solid catalyst was elucidated by simultaneous atomistic RMC modeling of the experimental X-ray structure factor F($\boldsymbol{Q}$), the pair distribution

function (PDF) G(**r**), and the extended X-ray absorption fine structure (EXAFS) spectra, all backed up by a comprehensive set of complementary analytical and experimental *in situ*/*ex situ* data.

In addition to the methodological progress presented here, we discovered that Co-dppeO_2 represents the first Co-based disordered one-dimensional (1D) transition metal coordination polymer, based on flexible templating of cobalt centers by oxidized 1,2-bis(diphenylphosphino)ethane (dppeO_2) ligands.[30,31] Our study introduces 1D transition metal coordination polymers as a versatile, soft-templated[34-36] catalyst type that complements metal-organic frameworks[37-39] and modern hybrid materials.[40-42,43,44]

In the following, we unravel how the formation process of Co-dppeO_2 generates a unique polymer architecture of hydrophobic organic linkers connecting hydrophilic Co-hydroxide clusters, which are themselves surrounded by a network of hydrogen-bound H_2O molecules. This unexpected embedding of {H_2O-$Co_2(OH)_2$-OH_2} sites[45-49] is among the first examples of soft matter templating along the lines of photosystem II[50] that resulted in durable heterogeneous catalysts.

RESULTS

Analysis of Intermediate Species: *In situ* FTIR Spectroscopy and DFT Simulations

In an effort to identify the relevant species involved in the formation of Co-dppeO_2, the three phases of the synthesis, i.e., the initial reaction at ambient temperature, thermolysis, and oxidation, were followed using *in situ* Fourier-transform infrared (FTIR) spectroscopy. Spectral peaks were then compared with computed spectra from an ensemble of optimized candidate molecules. Potential cobalt-CO-dppe complexes were modeled by DFT at the ωB97XD/def2SVP level of theory and with solvation in mesitylene using a continuum dielectric method (for details of calculations, see Supplemental Experimental Procedures). The ωB97XD density functional was chosen as it contains long-range exchange and dispersion corrections and has been successfully used in the studies of transition metal compounds.

In the initial mixture, dppe reacted rapidly with a slight excess of $Co_2(CO)_8$ in deoxygenated mesitylene at 24 °C under 50 psi of CO, converging to a complex but stable mixture of cobalt carbonyl species, and a modest elevation of pressure in the system. In addition to some remaining $Co_2(CO)_8$, the major species in this mixture appear to be **A1** ($[CoCO_4]^-$), **A2** ($[Co(dppe)(CO)_2]^+$) and possibly **A6** ($[Co(dppe)(\mu\text{-}CO)(CO)]_2^{2+}$).

As shown in Figure 1A, the broad peak observed at ≈1920–1820 cm^{-1} matches the asymmetric metal-bound C-O stretching vibration of **A1** at ≈1900 cm^{-1} and both asymmetric and symmetric C-O stretching vibrations for carbonyls bridging the Co centers of **A6** at ≈1905 and ≈1882 cm^{-1}, as well as residual $Co_2(CO)_8$. The peak seen

at ≈2085 cm^{-1} matches very well with the symmetric C-O stretching vibration of terminal carbonyls for both **A2** and **A6**, while the peak at ≈2036 cm^{-1} matches the asymmetric C-O stretching vibration for both **A2** and **A6**. Together, these species account for all observed carbonyl peaks in the spectrum, except for the peak at ≈1950 cm^{-1}, which may indicate presence of a μ-CO, but all calculated structures with excellent overlap in this region have significant deviations in other areas (see Supplemental Information for details).

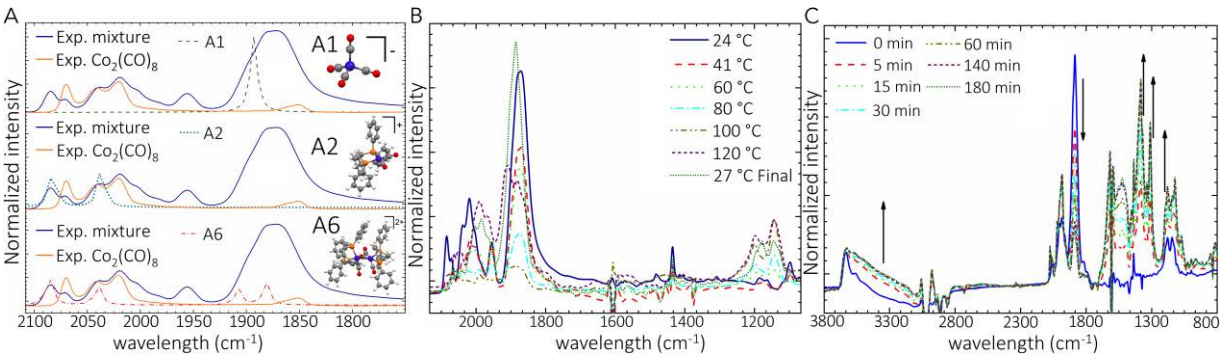

Figure 1. *In Situ* and DFT Calculated IR Spectra for Potential Co-CO-dppe Intermediates
(A) *In situ* IR spectra at the start of the reaction at 24 ºC with the DFT calculated IR spectra for candidate molecules **A1**, **A2**, **A6**; IR spectra were calculated with ωB97XD/def2svp level of theory in mesitylene.
(B) *In situ* IR spectra at increasing temperatures.
(C) *In situ* IR spectra for the oxidation time course.

Thermolysis of the reaction followed. The reactor was heated by 20 °C increments, allowing 20–120 min for the spectrum to stabilize after each temperature change. From 24 °C until 100 °C only minor changes were observed, but at 120 °C there was an evident increase in complexity of the spectrum, including new strong peaks at ≈1990 and ≈1905 cm^{-1} and nearly complete disappearance of peaks ascribed to terminal carbonyls in **A2** and/or **A6** (Figure 1B). This is particularly interesting because previous studies[30,32] found material produced in refluxing toluene (bp 110°C) to be chemically distinct and catalytically inferior to material produced in refluxing xylenes (bp 142 °C). Because toluene, xylenes and mesitylene all have similar properties as solvents, it is likely that reactions occurring above the boiling point of toluene are crucial to the formation of active catalyst. After cooling back to 27 °C, the IR spectrum was noticeably different from that observed before thermolysis, lacking peaks ascribed to terminal carbonyls in **A2** and/or **A6**.

At this point, the CO atmosphere was vented, and replaced with 25 psi of dry O_2, to oxidize the intermediate product. This resulted in an increase in vibrations assigned to phosphine oxides (≈1200–1000 cm^{-1}) (Figure 1C), and the appearance of peaks attributed to O-H stretching and bending modes (≈3685-3150 and ≈1700–1260 cm^{-1}), as well as a marked overall decrease in carbonyl signal intensity (Figure 1C). There are multiple documented examples of cobalt-tertiary phosphine complexes reacting selectively with dioxygen to produce the corresponding cobalt-tertiary phosphine oxide complexes with high selectivity.[51,52,53,54] Both PO and residual CO signals appear

to match well with calculated spectra for $Co(CO)_2$ centers with phosphine oxide ligands (see Supplemental Information for computed structures and spectra). After 3 h under 25 psi O_2 and then 70 h under air at ambient pressure, the precipitate was purified using the same method employed in preparative synthesis, and the IR spectrum of the resulting material matched the spectra found for the final purified Co-dppeO_2 complex used in all *ex situ* studies (Figure S1).

Structure of the Final Purified Co-dppeO_2 Solid Catalyst

Understanding the topologically disordered structure of Co-dppeO_2 sets an essential example for future rationalization and exploitation of the structure-activity relationships involved in electrochemical reactions of disordered hybrid organic-inorganic coordination systems. However, the absence of systematic and well-established methods to accomplish such complex tasks still poses great challenges.

An earlier study[31] has shown that the structure of Co-dppeO_2 cannot be resolved from standard X-ray diffraction refinement, because the diffraction pattern only exhibits broad and low intensity diffraction signals arising from the dppeO_2 ligand. This renders the determination of the structure of Co-dppeO_2 quite difficult, beyond the qualitative suggestion that it represents a disordered catalyst containing traces of crystalline dppeO_2. Here, the topological atomic short-range order of Co-dppeO_2 is deciphered from RMC modeling using an input model structure to simultaneously fit the structure factor F($\boldsymbol{Q}$), the pair distribution function G($\mathbf{r}$), and the EXAFS spectra extracted from measured high-energy synchrotron X-ray total scattering and XAS data.

The local-structure of the hydrophobic bis-phosphine oxide bridging the cobalt clusters is obtained from fitting the F($\boldsymbol{Q}$) and G($\mathbf{r}$) functions. The statistics of many-body correlations in the nearest coordination shells around catalytically active cobalt centers is more precisely extracted from fitting the EXAFS spectra. This unified approach allows a seamless correlation between different experimental data offering structural insights at multiple atomic length scales, thus providing a realistic 3D model of the disordered structure of Co-dppeO_2, which cannot be achieved from conventional crystallographic analysis.

For RMC modeling, the input model motif was built in line with structural insights acquired from the comprehensive analyses of complementary *ex situ* X-ray photoelectron spectroscopy (XPS), NMR, thermogravimetric analysis, IR, and Raman characterizations of the synthesized Co-dppeO_2 catalyst (for details see the Supplemental Information). First, measured *ex situ* XPS C 1s spectra (Figure S5), display the C-C, C-H and C-P bonds of the dppe ligand, and exclude the presence of carbonates. XPS P 2p spectra suggest P-O bonding most consistent with tertiary phosphine oxide functionality,[55] and the O 1s spectra indicate the chemical state of oxygen involving OH groups. Furthermore, *ex situ* ^{31}P NMR spectra show two isotropic signals at ≈33.4 and ≈34.9

ppm, consistent with having one molecule of oxidized dppeO$_2$ ligand. The dppeO$_2$ ligands are coordinated via their O atoms to two Co-centers (Figure S6). Elemental analysis suggested the presence of 15 wt% of water (confirmed by Karl Fischer titration), and a stoichiometry of two cobalt atoms per molecule of dppeO$_2$ ligand (Figure S7 and Table S5). Direct comparison of the absorption edge energy-position in the XANES spectra of Co-dppeO$_2$ with that of reference compounds (Co-metal, LiCo^{III}O$_2$, and Co^{II}O) indicates that most Co sites hold the Co^{II} valence state (see inset of Figure 2G).

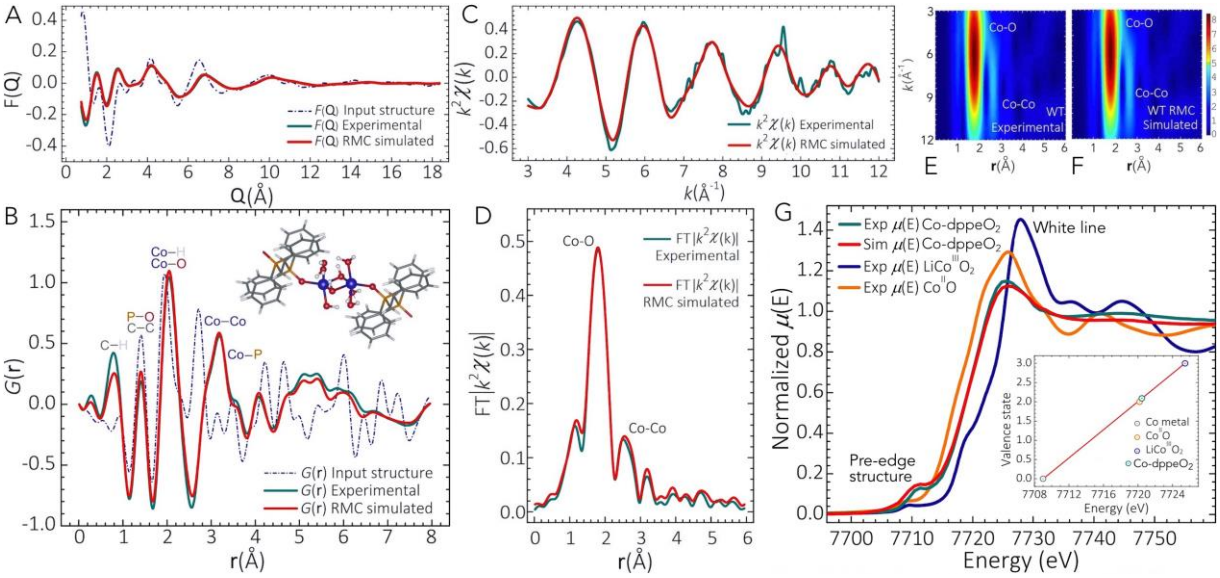

Figure 2. RMC Modeling of the Structure of the Final Purified Co-dppeO$_2$ Solid Catalyst
(A and B) RMC simulations (red line) of the experimental F(***Q***), G(**r**) spectra of Co-dppeO$_2$ (green line). The dotted curves correspond to the calculated F(***Q***), G(**r**) functions of the input model structure.
(C and D) RMC simulations (red line) of the experimental $k^2\chi(k)$ and FT|$k^2\chi(k)$| spectra of Co-dppeO$_2$ (green line, phase-uncorrected).
(E and F) 2D-contour plots of the experimental and RMC simulated WT of the $k^2\chi(k)$ spectra.
(G) Experimental XANES spectra (green line) and the calculated one from the RMC optimized structure of Co-dppeO$_2$ by *ab-initio* methods (red line). The XANES spectra of reference compounds LiCo^{III}O$_2$ and Co^{II}O are also shown and used for estimation of the Co^{II} valence state in the inset.

Taking this structural information into account, an input model motif of Co-dppeO$_2$ was established, consisting of oxidized dppeO$_2$ ligands linking {Co$_2$(μ-OH)$_2$(OH)$_2$(H$_2$O)$_2$} clusters enclosed by hydrogen-bonded water molecules (see inset of Figure 2B). From this model motif an extended input 3D-model structure of Co-dppeO$_2$ was built by linking different dppeO$_2$-{Co$_2$(μ-OH)$_2$(OH)$_2$(H$_2$O)$_2$}-dppeO$_2$ clusters. Figures 2A and 2B contrasts the F(***Q***) and G(**r**) functions as calculated from the input model structure against the experimental spectra, showing that the input Co-dppeO$_2$ model structure nearly reproduces the measured spectral features of the experimental data.

Results from RMC optimization of the input Co-dppeO$_2$ model structure attain good fit to the measured F(***Q***) and G(**r**) spectra, replicating all relevant spectral features of the experimental data (Figures 2A and 2B). Main interatomic distances are given in the Table S6. The RMC simulated EXAFS $k^2\chi(k)$ and FT|$k^2\chi(k)$| spectra and its

wavelength transform (WT) reproduce the experimental *k*- and real-space position at r≈1.82 Å [*k*≈6.2 $Å^{-1}$] and r≈2.54 Å [*k*≈7.3 $Å^{-1}$] arising from backscattering by neighboring O and Co atoms sited at the first-second coordination shells from the photoabsorbing Co centers (Figures 2C-2F).

The RMC optimized structure shows that the atomic short-range topology of Co-dppeO_2 comprises of a coordination polymer consisting of hydrophobic bis-phosphine oxide dppeO_2 ligands connected to each other by bridging hydrophilic {Co_2(μ-OH)$_2$(OH)$_2$(H_2O)$_2$} clusters surrounded by H-bound H_2O molecules (Figures 3A and 3B). The Co atoms adopt a distorted square pyramidal pentacoordinate environment consisting of neighboring O atoms, one of which belongs to the dppeO_2 ligand. While the structure of Co-dppeO_2 appears to hold a well-defined atomic short-range topology into the metal-to-ligand environment, the molecular structure of the dppeO_2 ligands is disordered between two relative molecular orientations (Figure 3B and Figure 5). This finding is consistent with the ^{13}C NMR spectra, which show two signals at ≈22.6 and ≈24.9 ppm, assigned to the CH_2 groups of the phosphine dppeO_2 ligands. The low number of phenyl ring resonances is evidence for disordered and still mobile aromatic carbon sites, as expected for such type of terminal groups (Figure S6). While these two disordered dppeO_2 molecular orientations are uniformly distributed in the topological structure of Co-dppeO_2, the $(CH_2)_2$ chain displays anti-conformation, with the P=O groups in a given molecule oriented antiparallel to each other, so that – independent of the relative molecular orientation of the dppeO_2 ligands–they are bridged by rotated and distorted {Co_2(μ-OH)$_2$(OH)$_2$(H_2O)$_2$} clusters.

Structural stability of the key structural motif of Co-dppeO_2 was further evaluated by DFT optimization (Figure 3C). Structural relaxation the Co-dppeO_2 motif conserves its atomic short-range topology, with dppeO_2 ligands linked to each other by bridging hydrophilic distorted {Co_2(μ-OH)$_2$(OH)$_2$(H_2O)$_2$} clusters surrounded by H-bound H_2O molecules. While additional rotations of the dppeO_2 ligands are observed, their occurrence will depend largely on structural packing, as they are more likely to arise *in silico* due to the degrees of freedom of the single molecule used during DFT optimization. Additionally, the distorted CoO_5 units give rise to the pre-edge structure observed in the Co *K*-edge XANES spectra of Co-dppeO_2 (Figure 2G), whose relative energy position and intensity are well reproduced from *ab initio* simulations from the RMC optimized structure of Co-dppeO_2. Since XANES spectra are sensitive to interatomic-distances/angles and atomic coordination environments, these findings further support the simulated atomic range order around the photoabsorbing Co atoms to properly reflect those present in the structure of the final purified Co-dppeO_2 solid catalyst.

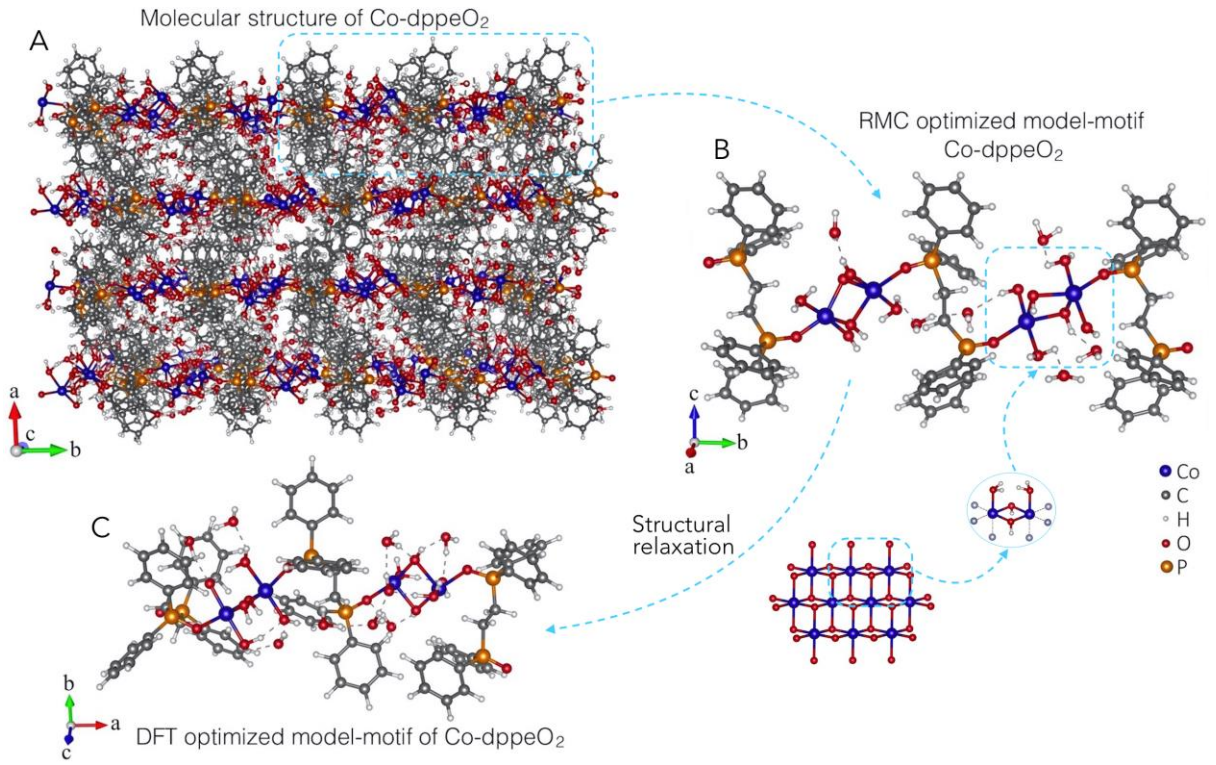

Figure 3. RMC Optimized Structure of Co-dppeO$_2$
(A and B) RMC optimized structure of final purified Co-dppeO$_2$ solid catalyst comprising a coordination polymer consisting of hydrophobic bis-phosphine oxide dppeO$_2$ ligands linked by bridging distorted hydrophilic oxocluster motifs {Co$_2$(μ-OH)$_2$(OH)$_2$(H$_2$O)$_2$} surrounded by H-bound H$_2$O molecules.
(C) DFT optimized structure showing the molecular stability of Co-dppeO$_2$ upon structural relaxation.

The hydrogen-bonded network of water molecules in Co-dppeO$_2$, enabled by the dppeO$_2$ soft template, is a key differentiator between the active site in this catalyst and cobalt oxide. Cobalt oxide is less active than many amorphous catalysts,[12] but we show that in this case, both possess a substantially similar active site. Just as delivery of water and egress of protons to the active site of photosystem II is facilitated by a proton relay that involves an adjacent tyrosine proton acceptor with a long-range water hydrogen-bonded network,[56] which has been shown to be a critical factor in the high activity of the oxygen evolution reaction (OER) in photosystem II,[57] in this system, we suggest that hydrophobic ligands in Co-dppeO$_2$ serve to channel water (and protons) to (and from) the hydrophilic active sites. Additional structural flexibility allows for efficient binding of substrate waters and rapid catalysis concomitant with rapid transport of substrate water, product protons and O$_2$ gas. Under longer operational periods, or in harsh environments, the hydrophobic dppeO$_2$ ligands can act as a soft template to optimize distribution of degradation products (such as CoO$_x$). This can explain the observed operational stability,[30] regardless of the structural stability of the ligand configuration over long periods of time.

Vibrational Properties of Co-dppeO$_2$

The experimental FTIR spectrum of Co-dppeO$_2$ was compared with simulated IR spectra calculated using the ωB97XD/def2SVP level of theory with solvation in mesitylene (Figures 4A and 4B) from model structures

generated de novo **A27** and using RMC-derived model motifs **A28** and **A29** (Figure S8). Comparison of the vibrational modes computed directly from complexes **A27**, **A28** and **A29** with the experimental spectra of Co-dppeO_2 are given in the Table S7. The fingerprint portion of the IR spectra in the range ≈1200-400 cm^{-1} is very complicated to assign, as several vibrational modes from the C-C, C-H and O-H stretching and bending motions are overlapping. However, the simulated and experimental spectra appear to be in general agreement, showing analogous line shape features (Figure 4B). The IR spectra calculated from model structures **A27**, **A28** and **A29** partially match the P-O stretching vibrational modes observed in the experimental spectra at ≈1175, ≈1069 and ≈1040 cm^{-1} (Table S7). The simulated Co-O stretching vibrations at ≈510-530 cm^{-1} from the **A28** and **A29** model motifs match the two peaks of the Co-dppeO_2 IR spectra in this region (Figure S9). However, these calculated vibrations are lower in intensity and closely overlap with the C-C, C-H, and O-H vibrations. It should be noted, however, that the **A27**, **A28** and **A29** model motifs only represent discrete snapshots of the multiple distorted units having different bond lengths and bond angles in the final Co-dppeO_2 product. Since the structures of these model motifs are different due to the various conformational arrangements of the ligands around the Co centers, shifts in vibrational modes are reflected on the calculated spectra for each model **A27**-**A29** (Figure 4B).

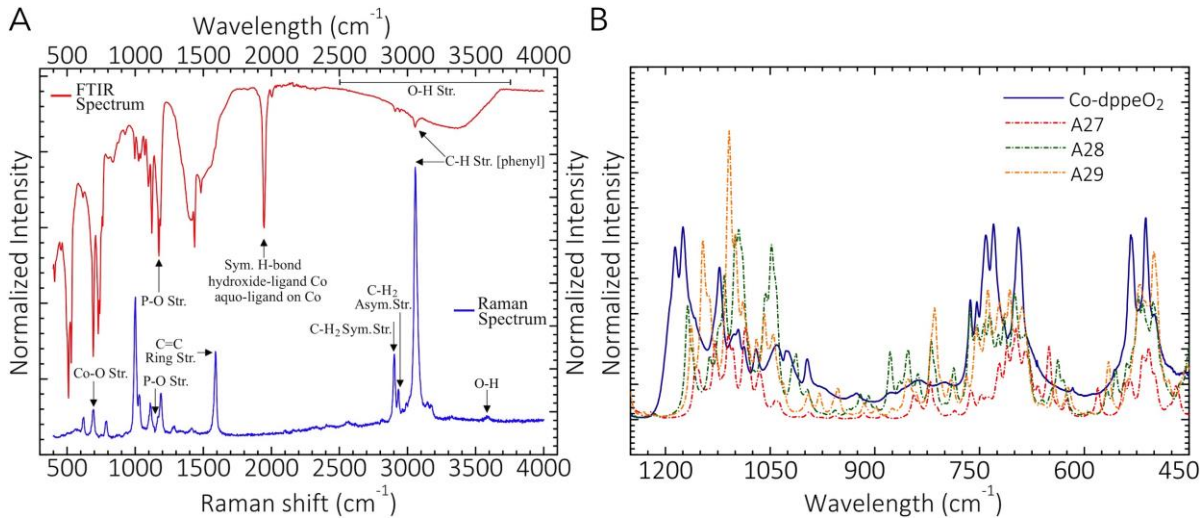

Figure 4. *Ex Situ* FTIR and Raman Spectra of Co-dppeO_2
(A) *Ex situ* FTIR and Raman spectra of Co-dppeO_2 showing transitions mainly from the dppeO_2 ligand.
(B) Fingerprint region of the FTIR spectra of Co-dppeO_2 vs the ωB97XD/def2svp calculated IR spectra from **A27**, **A28** and **A29** model structures.

Therefore, while similarities between the IR spectra calculated from **A27**, **A28** and **A29** model motifs and the experimental IR spectrum of the final Co-dppeO_2 complex in these fingerprint regions can be observed, its IR spectrum should be an average of all possible combinations of the aqua, hydroxy and dppeO_2 ligand environments around the Co centers. Although the broad feature observed at ≈1950 cm^{-1} in the experimental IR spectrum (Figure 4A) appears to be in the right region for a cobalt-bound carbonyl stretching vibration, ^{13}C NMR spectra did not

offer any evidence of carbonyls (Figure S6). Additionally, the peak survived light-driven water oxidation under strongly alkaline conditions in a parallel study (Figure S10), which would be highly unusual for the easily oxidized carbonyl moiety. Interestingly, the peak disappears within hours when the catalyst is stored in the presence of a desiccant, but is stable under a humid atmosphere for weeks, suggesting the involvement of water (unfortunately, disappearance of this peak is irreversible, and treatment with H_2O or D_2O does not change this region of the IR spectrum further). A possible assignment for this vibration could be ascribed to a symmetrical hydrogen bond between a cobalt-bound water molecule (H donor) and a hydroxide ion bound to the neighboring cobalt center (H acceptor). This motif appears in several computed models, and in the case of structure **A27**, DFT calculations predict a stretching frequency of ca. ≈1930 cm^{-1} for this O–H•••O bond (Figure S11).

Ex situ Raman spectra of Co-dppeO_2 show transitions mainly arising from the organic dppeO_2 ligand (Figure 4A). Characterization of the vibrational modes is presented in Table S8. Comparing the Raman spectra of Co-dppeO_2 with that of reference compounds (CoOOH, $Co(OH)_2$, Ph_3PO, Co_3O_4, CoO) (Figures S12 and S13), ruled out the presence of adventitious cobalt oxide particles in the dppeO_2 organic ligand-matrix, because the oxide peaks are absent in the Raman spectra of Co-dppeO_2.

This agrees with HRTEM images, which show a disordered microstructure without traces of cobalt oxide particles (Figure S14). The vibrational band at ≈692 cm^{-1} in the Raman spectra of Co-dppeO_2 is due to overlapping of Co-O stretching modes of distorted $\{Co_2(\mu\text{-}OH)_2(OH)_2(H_2O)_2\}$ units and out-of-plane sextant ring deformation modes of the dppeO_2 ligand. The vibrational bands at ≈1169 cm^{-1} and ≈3587 cm^{-1} arise from P-O stretching and OH vibrational modes, respectively (Figure 4A). Based on the FTIR-Raman spectra, the C-H and C-C bond-lengths were estimated from bond length stretching frequency correlations. Thus, the stretching frequencies at ≈3057-3059 cm^{-1} and ≈1590 cm^{-1} relate to bond lengths of C-H≈0.98±0.02 Å and C-C≈1.40±0.02 Å, respectively, which agree with those calculated from RMC modeling of the experimental F($\boldsymbol{Q}$) and G(**r**) functions (Table S6).

DISCUSSION

The compositional and structural properties of Co-dppeO_2 clearly indicate that its structural features differ fundamentally from cobalt oxide catalysts. In general terms, the structural elucidation of Co-dppeO_2 demonstrates the great potential of disordered hybrid materials to combine critical motifs of inorganic materials with hydrogen-bonded organic environments. Our cohesive methods that unify experimental *in situ*/*ex situ* spectroscopic data and theoretical modeling reveal the presence of a complex and disordered 1D-coordination polymer architecture in Co-dppeO_2 (Figure 3 and Figure 5).

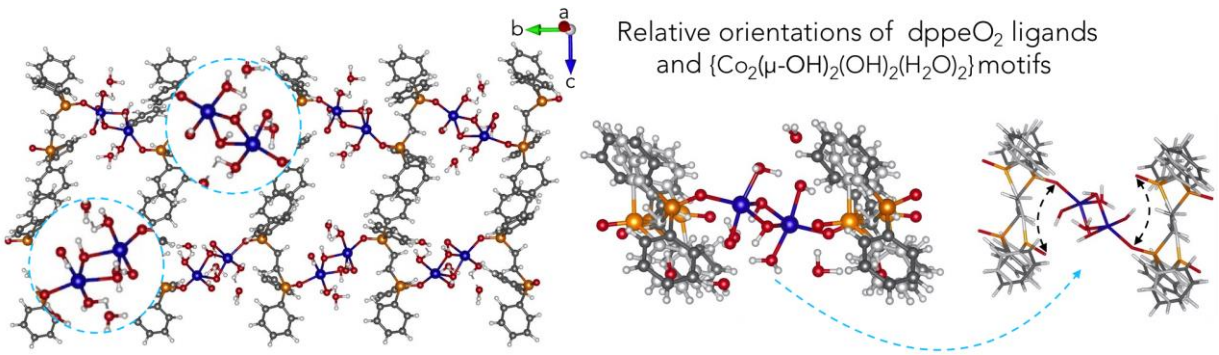

Figure 5. Rotational Disordered Moieties of Co-dppeO$_2$ and {H$_2$O-Co$_2$(OH)$_2$-OH$_2$} Edge Site
Molecular structure of the final purified Co-dppeO$_2$ solid catalyst showing the two relative orientations of the dppeO$_2$ ligands with the bridging distorted hydrophilic oxocluster motifs {Co$_2$(μ-OH)$_2$(OH)$_2$(H$_2$O)$_2$}.

The key structural motif of Co-dppeO$_2$, namely hydrophobic dppeO$_2$ ligands bridging hydrophilic distorted edge-site {Co$_2$(μ-OH)$_2$(OH)$_2$(H$_2$O)$_2$} clusters (Figure 3),[45,46,58] each surrounded by a network of hydrogen-bonded water molecules, emerged as the highest-performing catalyst after screening > 20 ligands with Co$_2$(CO)$_8$ as a cobalt source (Figure 5).[30] Most importantly, the embedding of the dicobalt units into the flexible and pre-oxidized dppeO$_2$ environment bears a striking functional resemblance to the OEC and related biological systems.[50,59] Therein, active hydrophilic metal-oxo cluster sites are embedded within a flexible scaffold allowing for transport of substrate water molecules to the cluster, while acting as a soft template for structural evolution. In addition, the flexibility of the organic ligands holding the {Co$_2$(μ-OH)$_2$(OH)$_2$(H$_2$O)$_2$} active sites in place enable adaptable Co-O bond lengths and atom efficiency that are not provided by the more rigid cobalt oxide lattice.

Since the local conformation of the polymer, the distribution of water molecules, and the potential stereoisomerism at cobalt have a significant number of degrees of freedom, disordered Co-dppeO$_2$ must be treated as an ensemble of closely related, but non-identical, monomers. Bottom-up DFT models converge to discrete examples of these possible monomeric units, while longer-range order RMC simulations converge to their "average" structures. Given the agreement found between the results from computational modeling and experimental data on multiple aspects, including the complex distribution of interatomic distances (PDF, EXAFS), vibrational frequencies (FTIR, Raman), and the electronic structure (XPS, XANES), we are quite confident in our structural assignments in Co-dppeO$_2$ and in the validity and consistency of the methods herein.

It has been shown previously that the mode of action and relative activity of Co-dppeO$_2$ in phosphate and borate electrolytes is different from CoO$_x$ and Co$_3$O$_4$.[30,31] The performance durability[30] of Co-dppeO$_2$ leads us to propose several hypotheses pertaining to the structurally adaptive and pre-oxidized dppeO$_2$ ligand environment: (1) that it lends high efficiency to the hydrophilic active di-μ-oxo bridged cobalt site through assisting substrate H$_2$O transport, and (2) that hydrophobic dppeO$_2$ ligands act as a soft matrix-template to optimize the distribution

of highly-active possible structural degradation products. Hence, even if smaller amounts of cobalt oxides CoO_x and Co_3O_4 are formed during catalysis, the hydrophobic $dppeO_2$ ligands are likely to prevent their aggregation, thus avoiding electrode deactivation and sustaining the observed high catalytic activity over longer operational periods. Importantly, the number of low-nuclear molecular cobalt complexes explored as water oxidation catalysts remain rather limited to date, compared to their extensively studied heterogeneous Co-containing counterparts. Although pentacoordinate binuclear Co(II) complexes containing $Co_2O_3N_2$ motifs have been reported in previous studies,[60,61,62,63] to the best of our knowledge none of these materials have been investigated for their water oxidation catalytic activity. In contrast, pentacoordinate Co-species in solid-state water oxidation catalysts offer unsaturated and accessible edge sites with high affinity for OH^- species in alkaline electrolytes, which strengthens interaction with water molecules and improves electrochemical OER performance.[64,65] In the present case, the pentacoordinate Co(II) ions in our inorganic-organic hybrid material do indeed enable strategies to improve catalytic reactivity. Identifying these key structural motifs for Co-$dppeO_2$, furthermore, enables us to study their effect on the way O_2 is formed and subsequently removed from the system, which we will pursue by analyzing kinetics and thermodynamics of this reaction using DFT in our future studies.

With such new structural insight into the key functional components of a flexible hybrid catalyst class at hand, we believe that this work will stimulate the informed exploration of this unlimited toolbox of disordered systems for water oxidation catalysis and beyond. Tailored geometry and hydrophobicity of the linking ligands hold the key to controlling the water networks, while the electronic properties of the clusters can be fine-tuned through appropriate metal-binding termini. This concept opens the door to new 1D, 2D, or 3D coordination polymers, exploiting the role of disorder and flexibility in material resilience.

Unveiling the atomic-range structure of disordered and dynamic materials has been a challenging and long-standing task in fundamental and applied research. Modern catalysis now requires creative approaches to resolve the detailed topological structure of their active centers to close the widening gap between empirical catalyst development and conceptual understanding. To this end, the comprehensive computational modeling and analytical *in situ*/*ex situ* characterizations used in this work can be further extrapolated to any disordered material to unravel its complex atomic-range structure from the bottom-up. Such insight is vital for unleashing the unlimited application potential of robust and low-cost disordered catalysts for a sustainable economy.

EXPERIMENTAL PROCEDURES

Materials Synthesis

Synthesis of the **Co-dppeO$_2$** catalyst was carried out following the protocol previously described in Lam et al.,[32] using as reagents dicobalt octacarbonyl, $Co_2(CO)_8$ (345 mg, 1.01 mmol), and 1,2-bis(diphenylphosphino)ethane, denoted dppe (399 mg, 1.00 mmol). Further details on the synthetic procedures of reference compounds can be found in Supplemental Information.

FTIR and Raman Spectroscopy

FTIR spectroscopy was performed using a Bruker Vertex 70 spectrometer equipped with a Pt attenuated total reflection (ATR), in transmittance mode. Raman spectra were recorded using a Renishaw Ramascope 1000 spectrometer equipped with a 780-nm diode laser from Renishaw with 50 mW capacity. To improve the signal to noise ratio, we used detection times of about 120 s.

In situ FTIR Spectroscopy

The FTIR instrument used for the in situ study is a Bruker Tensor 27 equipped with a mid-IR source, swappable room-temperature deuterated triglycine sulfate detector, and liquid nitrogen-cooled narrow-band mercury-cadmium-telluride (MCT) detectors. The MCT detector was used with the SpectraTech high-pressure IR cell. The Bruker OPUS program (version 7.2.139.1294) was used for data collection and data analysis on a Windows 7 computer system. The higher IR throughput of the ZnSe crystal led us to use a 2-mm aperture setting to avoid oversaturating the MCT detector. Background spectra with mesitylene solvent were collected and stored at the various temperatures planned for the sample spectra. Solvent backgrounds were then loaded and automatically subtracted from sample spectra at the corresponding temperatures. FTIR spectra were collected with the following parameters: 128 scans (background and sample), 4 cm^{-1} resolution, Blackman-Harris 3-term apodization, Mertz phase correction, zero filling factor = 2, and ATR intensity correction. Further details on the FTIR SpectraTech High-Pressure IR Cell spectrometer and experimental method can be found in Supplemental Information.

Synchrotron X-ray Total Scattering

The high-energy X-ray total scattering experiments were conducted at the beamline ID15A at the European Synchrotron Radiation Facility (ESRF) Grenoble. Data were collected at room temperature using high energy photons of 75 keV (λ=0.164 Å), with appropriate statistics to achieve high momentum transfer values $\boldsymbol{Q}$ ($\boldsymbol{Q}_{max}=4\pi\sin\theta/\lambda$). Solid samples were packed into Kapton tubes with inner diameter of 1.5 mm and mounted in transmission geometry. The intensity scattered from the unfilled Kapton tubes was measured separately for background subtraction. Intensities were recorded using a PILATUS3X CdTe 2M solid-state detector with sample-to-detector distance of ≈200 mm. The experimental 2D images were processed using the pyFAI program[66] to yield 1D ($\boldsymbol{Q}$, **I**) diffraction patterns. The PDFgetX3 program[67] was used to subtract the background (empty Kapton tube), to perform instrument and sample corrections, and to obtain the corrected-normalized diffraction intensity of the total scattering structure factor $S(\boldsymbol{Q})$ and the X-ray structure factor $F(\boldsymbol{Q})$. The $S(\boldsymbol{Q})$ was converted into the pair distribution function (PDF), $G(\mathbf{r})$, through the sine-Fourier transform according to

$$G(\mathbf{r}) = \frac{2}{\pi}\int_{\boldsymbol{Q}_{\min}}^{\boldsymbol{Q}_{\max}} \boldsymbol{Q}[S(\boldsymbol{Q}) - 1]\sin \boldsymbol{Q}\mathbf{r}d\boldsymbol{Q},$$

$G(\mathbf{r})$ represents the probability of finding an atom *i* at a given distance **r** from another atom *j*. The relative intensity in $G(\mathbf{r})$ relates directly to the number of these pairs and their scattering power. For amorphous materials, the intensity in $G(\mathbf{r})$ peaks diminish as **r** increases due to the finite range of structural correlations and defines the atomic-range order in the material.

X-ray Absorption Spectroscopy

Experiments were performed at the SuperXAS beamline of the Swiss Light Source (SLS), Villigen, Switzerland, on solid samples dispersed in cellulose at room temperature. The storage ring was run in the top-up mode with an average current of 400 mA. The X-ray beam was collimated by a Si coated mirror and the energy was scanned by a channel-cut Si[111] monochromator. Energy calibration was performed using metal Co foil (with the maximum of the first derivative of the spectrum at 7709 eV). A toroidal mirror with Rh coating was employed after the monochromator to focus the incident X-rays with a spot size of 140×120 μm^2 on the sample. Measurements on **Co-dppeO$_2$** tablet-shaped samples were performed in transmission mode. Absorption-edge-energy calibration, background subtraction, data reduction and analyses of the extracted EXAFS, $k^2\chi(k)$, and Fourier transform, FT|$k^2\chi(k)$|, spectra were performed using the Athena and Artemis programs as implemented into the IFEFFIT software package.[68]

Density Functional Theory Calculations

All calculations were performed using the Gaussian 09 (revision d.01)[69] suite programs. Ground-state geometries were optimized in mesitylene employing the self-consistent reaction field (SCRF) method via the polarized continuum solvation model[70] with the ωB97XD[71] density functional and the def2SVP[72,73] basis set. The optimized geometries were then used in vibrational frequency calculations. Obtained frequencies were then subsequently scaled by a factor of 0.9394. A pruned integration grid with 75 radial shells and 302 angular points per shell (the G09 default fine grid) was used for all calculations. Further details on the calculations can be found in Supplemental Information.

Atomistic Reverse Monte Carlo Modeling

To simulate the atomic short-range topology in the molecular structure of Co-dppeO$_2$, an extended input 3D-model structure of Co-dppeO$_2$ consisting of dppeO$_2$-{Co$_2$(μ-OH)$_2$(OH)$_2$(H$_2$O)$_2$}-dppeO$_2$ clusters, was fitted to the experimental $F(\boldsymbol{Q})$ [$\Delta\boldsymbol{Q}$≈1-18 Å^{-1}], $G(\mathbf{r})$ [$\Delta\mathbf{r}$≈0-8 Å] and $k^2\chi(k)$ [Δk≈3-12 Å^{-1}], FT|$k^2\chi(k)$| [$\Delta\mathbf{r}$≈0-6 Å] spectra by RMC simulations, as implemented in RMCProfile.[74] From prior EXAFS fitting by ARTEMIS[68] the threshold energy shift was set to ΔE_0≈-0.59 eV and S_0^2≈0.9. The atoms were constrained to move into cutoff distances C-C≈1.38-1.46 Å, C-H≈0.96-1.02 Å, Co-O≈2.0-2.4 Å, Co-Co≈2.9-3.4 Å, Co-P≈3.0-3.4 Å, O-P≈1.52-1.72 Å, O-H≈0.96-0.99 Å. To conserve the bonding of aromatic C-H rings and H$_2$O molecules, the stretching potentials: C-C 4.08 eV (1.42 Å), C-H 3.66 eV (0.96 Å), O-H 3.43 eV (0.98 Å) were used, and their weightings were optimized at each RMC cycle. The input model-structure of Co-dppeO$_2$ was then optimized by RMC modeling by allowing 1-3% of atoms to undergo displacements of ≈0.01-0.08 Å at each RMC cycle. Total $k^2\chi(k)$, FT|$k^2\chi(k)$| RMC functions equal to the averaged single spectrum of each photoabsorbing Co atom were recalculated at each RMC run. Convergence to a minimum residual was attained by running ≈1×10^6 RMC cycles. Each atomic movement was tested according to the degree of consistency R^2 between the experimental and refined spectral-data-points as described in detailed references.[75,76,77,78]

***Ab initio* Calculations of XANES Spectra**

Ab initio simulations of the Co *K*-edge XANES spectra for the RMC optimized molecular structure of Co-dppeO$_2$ were done self-consistently by finite difference method as implemented in the near-edge structure FDMNES code.[79] The real self-energy-dependent exchange potential by Hedin-Lundqvist was used. The final excited state was approached by relaxed configurations with a core-hole at the 1*s* level and an extra electron at the 4*p* level. Single Co *K*-edge signals were computed on a grid of 7 Å centered at each Co center and averaged to total XANES spectra.

Further details on the complementary analytical characterization can be found in Supplemental Information.

DATA AND CODE AVAILABILITY

The authors declare that data supporting the findings of this study are available within the paper, the Supplemental Information, and the Experimental Procedures. All other data are available from the lead contact upon reasonable request.

SUPPLEMENTAL INFORMATION

Supplemental Information can be found online at https://doi.org/10.1016/j.matt.2019.06.021.

ACKNOWLEDGMENTS

G.R.P, C.A.T., and R.M. thank the University of Zurich, Switzerland, and the University Research Priority Program (URPP) for Solar Light to Chemical Energy Conversion (LightChEC) for financial support. G.R.P. is grateful to the Swiss National Science Foundation, Switzerland (Sinergia grant no. CRSII2_160801/1) for financial support. P.T.A. acknowledges support from QAFCO. E.N.B. and S.W.S. acknowledge support from the Qatar National Research Foundation, Qatar, under NPRP10-0125-170246. The authors thank Dr. Chi Chen for insightful discussions.

AUTHOR CONTRIBUTIONS

G.R.P., S.W.S., A.J.B., and P.T.A. conceived the research. C.A.T., P.V.P., E.N.B., and S.D.Z. performed the theoretical studies. A.J.B. and G.S. collected in situmonitoring data. R.M., T.F., and S.G.F performed structural and analytical characterizations. G.R.P., C.A.T., S.W.S., P.V.P., and A.J.B. wrote the manuscript. All authors analyzed the data and commented on the manuscript.

DECLARATION OF INTERESTS

US Patent No. 10,081,650B2, by A.J.B., S.W.S., and P.T.A., contains intellectual property described in the article. The other authors declare no competing.

REFERENCES

[1] Roger, I., Shipman, M. A. and Symes, M. D. Earth-abundant catalysts for electrochemical and photoelectrochemical water splitting. Nat. Rev. Chem. 1, 1-13 (2017).
[2] Montoya, J. H. Seitz, L. C., Chakthranont, P., Vojvodic, A., Jaramillo, T. F., and Nørskov, J. K. Materials for solar fuels and chemicals. Nat. Mater. 16, 70-81 (2017).
[3] Stamenkovic, V. R., Strmcnik, D., Lopes, P. P. and Markovic, N. M. Energy and fuels from electrochemical interfaces. Nat. Mater. 16, 57-69 (2017).
[4] Seh, Z. W., Kibsgaard, J., Dickens, C. F., Chorkendorff, I., Nørskov, J. K., Jaramillo, T. F., Combining theory and experiment in electrocatalysis: Insights into materials design. Science 355, 4998-5009 (2017).
[5] Vickers, J. W., Lv, H. Sumliner, J. M., Zhu, G., Luo Z., Musaev, D. G., Geletii, Y. V., and Hill, C. L. Differentiating homogeneous and heterogeneous water oxidation catalysis: Confirmation that $[Co_4(H_2O)_2(\alpha\text{-}PW_9O_{34})_2]^{10-}$ is a molecular water oxidation catalyst. J. Am. Chem. Soc. 135, 14110-14118 (2013).
[6] Kalz, K. F. Future challenge in heterogeneous catalysis: Understanding catalysts under dynamic reaction conditions. ChemCatChem. 9, 17-29 (2017).
[7] Eremin, D. B., and Ananikov, V. P. Understanding active species in catalytic transformations: from molecular catalysis to nanoparticles, leaching, “cocktails” of catalysts and dynamic systems. Coord. Chem. Rev. 346, 2-19 (2017).
[8] Fellet, M., and Tiede, D. Search for water-splitting catalysts for global usage. MRS Bulletin, 42, 190-194 (2017).

[9] Hartfelder, U., Singh, J., Haase, J., Nachtegaal, M., Grolimund, D., and van Bokhoven, J. A. Detecting and utilizing minority phases in heterogeneous catalysis. Scientific Reports 6, 37597 (2016).
[10] Lan, X., Hensen, E.J. and Weber, T., Silica-supported Ni_2P: effect of preparation conditions on structure and catalytic performance in thiophene hydrodesulfurization (HDS). Catalysis Today. 292, 121-132 (2017).
[11] Smith, R. D. L., Prévot, M. S., Fagan, R. D., Zhang, Z., Sedach, P. A., Siu, M. K. J., Trudel, S., Berlinguette, C. P. Photochemical route for accessing amorphous metal oxide materials for water oxidation catalysis. Science 340, 60-63 (2013).
[12] Indra, A., W. M. Prashanth, Sahraie, N. R., Bergmann, A., Das, C., Tallarida, M., Schmeißer, D., Strasser P., and Driess, M. Unification of catalytic water oxidation and oxygen reduction reactions: Amorphous beat crystalline cobalt iron oxides. J. Am. Chem. Soc. 136, 17530-17536 (2014).
[13] Surendranath, Y., Kanan, M. W., and Nocera, D. G. Mechanistic studies of the oxygen evolution reaction by a cobalt-phosphate catalyst at neutral pH. J. Am. Chem. Soc. 132, 16501-16509 (2010).
[14] Fabbri, E. Nachtegaal, M., Binninger, T., Cheng, X., Kim, B.-J., Durst, J., Bozza, F., Graule, T., Schäublin R., Wiles, L., Pertoso, M., Danilovic, N., Ayers, K. E., and Schmidt, T. J. Dynamic surface self-reconstruction is the key of highly active perovskite nano-electrocatalysts for water splitting. Nat. Mater. 16, 925-931 (2017).
[15] Kanan, M. W., Yano, J., Surendranath, Y., D. Mircea, Yachandra, V. K., and Nocera, D. G. Structure and valency of a cobalt-phosphate water oxidation catalyst determined by in situ X-ray spectroscopy. J. Am. Chem. Soc. 132, 13692-13701 (2010).
[16] King, H. J., Bonke, S. A., Chang, S. L. Y., Spiccia, L., Johannessen, B., and Hocking, R. K. Engineering disorder into heterogenite-like cobalt oxides by phosphate doping: Implications for the design of water-oxidation catalysts. ChemCatChem 9, 511-521 (2017).
[17] Zhang, K., Wang, L., Kim, J. K., Ma, M., Veerappan, G., Lee, C.-L., Kong, K., Lee, H., and Park, J. H. An order/disorder/water junction system for highly efficient co-catalyst-free photocatalytic hydrogen generation. Energy Environ. Sci., 9, 499-503 (2016).
[18] Cai, J., Zhu, Y., Liu, D., Meng, M., Hu, Z., and Jiang, Z. Synergistic effect of titanate-anatase heterostructure and hydrogenation-induced surface disorder on photocatalytic water splitting. ACS Catal. 5, 1708-1716 (2015).
[19] Huynh, M., Shi, C., Billinge, S. J. L., and Nocera, D. G. Nature of activated manganese oxide for oxygen evolution. J. Am. Chem. Soc. 137, 14887-14904 (2015).
[20] Sabri, M., King, H. J., Gummow, R. J., Lu, X., Zhao, C., Oelgemöller, M., Chang, S. L. Y., and Hocking, R. K. Oxidant or catalyst for oxidation? A study of how structure and disorder change the selectivity for direct versus catalytic oxidation mediated by manganese(III,IV) oxides. Chem. Mater. 30, 8244-8256 (2018).
[21] Bruckner, A. Spin–spin exchange in vanadium-containing catalysts studied by in situ-EPR: a sensitive monitor for disorder-related activity. Topics in Catalysis. 38, 1-3 (2006).
[22] Kwon, G., Kokhan, O, Han A, Chapman K. W., Chupas P. J., Du P, Tiede., D. M. Oxyanion induced variations in domain structure for amorphous cobalt oxide oxygen evolving catalysts, resolved by X-ray pair distribution function analysis. Acta Cryst. B 71, 713-721 (2015).
[23] Pandey, A., Biswas, P., and Drabold, D. A. Inversion of diffraction data for amorphous materials, Scientific Rep. 6, 33731 (2016).
[24] Strunk, J., Banares, M. A., and Wachs, I. E. Vibrational Spectroscopy of Oxide Overlayers. Top. Catal. 60, 1577-1617 (2017).
[25] Goldsmith, B. R., Peters, B., Johnson, J. K., Gates, B. C., and Scott, S. L. Beyond ordered materials. Understanding catalytic sites on amorphous solids. ACS Catal. 7, 7543-7557 (2017).
[26] Gibson, E. K., Beale, A. M., Catlow, C. R. A., Chutia, A., Gianolio, D., Gould, A., Kroner, A., Mohammed, K. M. H., Perdjon, M., Rogers, S. M., and Wells, P. P. Restructuring of AuPd nanoparticles studied by a combined XAFS/DRIFTS approach. Chem. Mater. 27, 3714-3720 (2015).
[27] Canton, S, Zhang, X. Lawson D. L., Smeigh, A., Zhang J., Liu, Y., Wallentin, C, Attenkofer, K., Jennings G., Kurtz, C.A., Gosztola, K. Warnmark, D., Hauser, A., and Sundstrom, V. Probing the anisotropic distortion of photoexcited spin crossover complexes with picosecond X-ray absorption spectroscopy, J. Phys. Chem. C, 118, 4536-4545 (2014).
[28] Seidler, G. T., Mortensen, D. R., Remesnik, A. J., Pacold, J. I., Ball, N. A., Barry, N., Styczinski, M., and Hoidn, O. R. A laboratory-based hard X-ray monochromator for high-resolution X-ray emission spectroscopy and X-ray absorption near edge structure measurements. Rev. Sci. Instrum. 85, 113906 (2014).
[29] Mathew, K., Zheng, C., Winston, D., Chen, C., Dozier, A., Rehr, J. J., Ong, S. P. and Persson, K. A. Data descriptor: High-throughput computational X-ray absorption spectroscopy. Scientific Data. 5, 180151 (2018).
[30] Bloomfield, A. J., Sheehan, S. W., Collom, S. L., Crabtree, R. H., and Anastas, P. T. A heterogeneous water oxidation catalyst from dicobalt octacarbonyl and 1,2-bis(diphenylphosphino)ethane. New J. Chem. 38, 1540-1545 (2014).
[31] Bloomfield, A. J., Sheehan, S. W., Collom, S. L., and Anastas, P. T. Performance enhancement for electrolytic systems through the application of a cobalt-based heterogeneous water oxidation catalyst. ACS Sustainable Chem. Eng. 3, 1234-1240 (2015).
[32] Lam, C.-H., Bloomfield, A. J., and Anastas, P. T. A switchable route to valuable commodity chemicals from glycerol via electrocatalytic oxidation with an earth abundant metal oxidation catalyst. Green Chem. 19, 1958-1968 (2017).
[33] Keane, T. P., Brodsky, C. N., and Nocera, D. G. Oxidative degradation of multi-carbon substrates by an oxidic cobalt phosphate catalyst. Organometallics. 38, 6, 1200-1203 (2019).
[34] Hasegawa, S., Horike, S., Matsuda, R., Furukawa, S., Mochizuki, K., Kinoshita, Y., and Kitagawa S. Three-dimensional porous coordination polymer functionalized with amide groups based on tridentate ligand: selective sorption and catalysis. J. Am. Chem. Soc. 129, 2607-2614 (2007).
[35] Kajiwara, T., Higashimura, H., Higuchi, M., and Kitagawa, S. Design and synthesis of porous coordination polymers with expanded one-dimensional channels and strongly Lewis-Acidic sites. ChemNanoMat 4, 103-111 (2018).
[36] Xing, B., Choi, M.-F., and Xu, B. Design of coordination polymer gels as stable catalytic systems. Chem. Eur. J. 8, 5028-5032 (2002).
[37] Miner, E. M., and Dinca, M. Metal-organic frameworks: Evolved oxygen evolution catalysts. Nat. Energy. 1, 1-2 (2016).

[38] Zhu, L., Liu, X.-Q., Jiang, H.-L., and Sun, L.-B. Metal-organic frameworks for heterogeneous basic catalysis. Chem. Rev. 117, 8129-8176 (2017).
[39] Zhang, H., Liu, X., Wu, Y., Guan, C., Cheetham, A. K., and Wang, J. MOF-derived nanohybrids for electrocatalysis and energy storage: current status and perspective, Chem. Commun. 54, 5268-5288 (2018).
[40] Zhang, R., Russo, P. A., Buzanich, A. G., Jeon, T., and Pinna, N. Hybrid organic-inorganic transition-metal phosphonates as precursors for water oxidation electrocatalysts. Adv. Funct. Mater. 27, 1703158 (2017).
[41] Li, D., Liu Z., Song J., Li H., Zhang B., Yin P., Zheng Z. N., Roberts J. E., Tsige M., Hill C. L., Liu T. Cation translocation around single polyoxometalate-organic hybrid cluster regulated by electrostatic and cation-p interactions. Angew. Chem. Int. Ed. 56, 3294-3208 (2017).
[42] Zhu, Y. P., Guo, C., Zheng, Y., and Qiao, S.-Z. Surface and interface engineering of noble-metal-free electrocatalysts for efficient energy conversion processes. Acc. Chem. Res. 50, 915-923 (2017).
[43] Mishra, R., Ülker, E., and Karadas, F. One dimensional copper(II) coordination polymer as an electrocatalyst for water oxidation. ChemElectroChem. 4, 75-80 (2017).
[44] Saha, J., Chowdhury, R. D., Jash, P., and Paul, A. Cobalt phosphonates as precatalysts for water oxidation: role of pore size in catalysis. Chem. Eur. J. 23, 12519-12526 (2017).
[45] Koroidov, S., Anderlund, M. F., Styring, S., Thapper, A., and Messinger, J. First turnover analysis of water-oxidation catalyzed by Co-oxide nanoparticles. Energy. Env. Sci. 8, 2492-2503 (2015).
[46] Zhang, M., de Respinis, M., and Frei, H. Time-resolved observations of water oxidation intermediates on a cobalt oxide nanoparticle catalyst. Nat. Chem. 6, 362-367 (2014).
[47] Risch, M., Ringleb, F., Kohlhoff, M., Bogdanoff, P., Chernev, P., Zaharieva, I., and Dau, H. Water oxidation by amorphous cobalt-based oxides: in situ tracking of redox transitions and mode of catalysis. Energy Environ. Sci. 8, 661-674 (2015).
[48] Song, F., Moré, R., Schilling, M., Smolentsev, G., Azzaroli, N., Fox, T., Luber, S., and Patzke, G. R. $\{Co_4O_4\}$ and $\{Co_xNi_{4-x}O_4\}$ cubane water oxidation catalysts as surface cut-outs of cobalt oxides, J. Am. Chem. Soc. 139, 14198-14208 (2017).
[49] Swierk, J.R., and Tilley, T.D. Electrocatalytic water oxidation by single site and small nuclearity clusters of cobalt. J. Electrochem. Soc. 165, H3028-H3033 (2018).
[50] Tanaka, A. Fukushima, Y., and Kamilla, N. Two different structures of the oxygen-evolving complex in the same polypeptide framework of photosystem II. J. Am. Chem. Soc. 139, 1718-1721 (2017).
[51] Heinze, K., Huttner, G., and Zsolnai, L. Cobalt-catalyzed selective oxidation of the tritertiary phosphane triphos with molecular oxygen. Chem. Ber./Recueil. 130, 1393-140 (1997).
[52] Fessler, M., Eller, S., Bachmann, C., Gutmann, R., Trettenbrein, B., Kopacka, H., Mueller, T., and Brueggeller, P. Regio- and chemoselective oxidation of the bis(bidentate) phosphine cis,trans,cis-1,2,3,4-tetrakis(diphenylphosphino)cyclobutane via cobalt(II) mediated dioxygen activation. Dalton Trans. 1383-1395 (2009).
[53] Kohl, S. W., Heinemann, F. W., Hummert, M., Weißhoff, H., and Grohmann, A. Tetra- and triphosphane pyridine podands and their cobalt(II) and nickel(II) complexes. Eur. J. Inorg. Chem. 16, 3901-3910 (2006).
[54] Saum, S. E. Askham, F. R., Fronczek, F. R., and Stanley, G. G. Reaction of oxygen with a binuclear cobalt(II) hexaphosphine complex. Single-crystal X-ray structure of an extended chain cobalt(II) hexaphosphine oxide system. Polyhedron. 7, 1785-1788 (1988).
[55] Strydom, C. A. X-ray photoelectron spectroscopy studies of some Cobalt(II) nitrate complexes. Inorganica Chimica Acta, 159, 191-195 (1989).
[56] Umena, Y., Kawakami, K., Shen, J.-R. and Kamiya, N., Crystal structure of oxygen-evolving photosystem II at a resolution of 1.9 Å, Nature 473, 55-60 (2011).
[57] Isobe, H., Shoji, M., Shen, J.-R., and Yamaguchi, K. Strong coupling between the hydrogen bonding environment and redox chemistry during the S_2 to S_3 transition in the oxygen-evolving complex of Photosystem II. J. Phys. Chem. B, 119, 13922-13933 (2015).
[58] Bergmann, A., Martinez-Moreno, E., Teschner, D., Chernev, P., Gliech, M., Araújo, J. F., Reier, T., Dau, H., and Strasser, P. Reversible amorphization and the catalytically active state of crystalline Co_3O_4 during oxygen evolution. Nat. Commun. 6, 8625 (2015).
[59] Lee, H. B., Shiau, A. A., Oyala, P. H., Marchiori, D. A., Gul, S., Chatterjee, R., Yano, J., R. Britt, D., and Agapie, T. Tetranuclear $[Mn^{III}Mn_3^{IV}O_4]$ Complexes as Spectroscopic Models of the S_2 State of the Oxygen Evolving Complex in Photosystem II. J. Am. Chem. Soc. 140, 17175-17187 (2018).
[60] Wang, T., Zhang, C., Ju, Z., and Zheng, H. Solvent-induced synthesis of cobalt(II) coordination polymers based on a rigid ligand and flexible carboxylic acid ligands: syntheses, structures and magnetic properties. Dalton Trans., 44, 6926-6935 (2015).
[61] Laugier, J., Ovcharenko, V., and Rey, P. Pentacoordinated binuclear complexes of cobalt(II) and nickel(II) with 3-imidazoline nitroxides. Inorganica Chimica Acta. 236, 49-53 (1995).
[62] Hoskins, B. F., and Williams, G. A. The crystal structure of a binuclear cobalt(II) complex of a macrocyclic ligand. Aust. J. Chem. 28, 2607-2614 (1975).
[63] Zeng, M.-H., Feng, X.-L., Zhang, W.-X., and Chen, X.-M. A robust microporous 3D cobalt(II) coordination polymer with new magnetically frustrated 2D lattices: single-crystal transformation and guest modulation of cooperative magnetic properties. Dalton Trans. 44, 5294-5303 (2006).
[64] Wan, H., Ma, R., Liu, X., Pan, J., Wang, H., Liang, S., Qiu, G., and Sasaki, T. Rare cobalt-based phosphate nanoribbons with unique 5-coordination for electrocatalytic water oxidation. ACS Energy Lett. 3, 1254−1260 (2018).
[65] Hu, C., Zhang, L., Zhao, Z.-J., Luo, J., Shi, J., Huang, Z., and Gong, J. Edge sites with unsaturated coordination on core–shell Mn_3O_4@$Mn_xCo_{3-x}O_4$ nanostructures for electrocatalytic water oxidation. Adv. Mater. 29, 1701820 (2017).
[66] Ashiotis, G., Deschildre, A., Nawaz, Z., Wright, J. P., Karkoulis, D., Piccac, F. E., and Kieffera, J. (2015). The fast azimuthal integration Python library: pyFAI. J. Appl. Cryst. 48, 510–519.
[67] Farrow, C. L., Juhas, P., Liu, J. W., Bryndin, D., Božin, E. S., Bloch, J., Proffen, Th., and Billinge, S. J. L. (2007). PDFfit2 and PDFgui: computer programs for studying nanostructure in crystals. J. Phys. Condens. Mat. 19, 335219.

[68] Ravel, B., and Newville, M. (2005). ATHENA, ARTEMIS, HEPHAESTUS: data analysis for X-ray absorption spectroscopy using IFEFFIT. J. Synchrotron. Rad. 12, 537-541.

[69] Frisch, M.J. *et al.* (2009). Gaussian 09, Revision D.01; Gaussian, Inc.: Wallingford, CT.

[70] Tomasi, J., Mennucci, B., and Cammi, R. (2005). Quantum Mechanical Continuum Solvation Models. Chem. Rev. 105, 2999–3093.

[71] Chai, J.-D., and Head-Gordon, M. (2008). Long-range corrected hybrid density functionals with damped atom-atom dispersion corrections. Phys. Chem. Chem. Phys. 10, 6615-6620.

[72] Weigend, F., and Ahlrichs, R. (2005). Balanced basis sets of split valence, triple zeta valence and quadruple zeta valence quality for H to Rn: Design and assessment of accuracy. Phys. Chem. Chem. Phys. 7, 3297-3305.

[73] Weigend, F. (2008). Accurate Coulomb-fitting basis sets for H to Rn. Phys. Chem. Chem. Phys. 8, 1057-1065.

[74] Tucker, M. G., Keen, D. A., Dove, M. T., Goodwin, A. L., and Hui, Q. (2007). RMCProfile: reverse Monte Carlo for polycrystalline materials. J. Phys.: Condens. Matter. 19, 1-16.

[75] Krayzman, V., Levin, I., Wocik, J. C., Proffen, T., Vanderah, T. A. and Tucker, M. G. A. (2009). Combined fit of total scattering and extended X-ray absorption fine structure data for local-structure determination in crystalline materials. J. Appl. Crystallogr. 42, 867-877.

[76] Németh, K., Chapman, K. W., Balasubramanian, M., Shyam, B. Chupas, P. J. Heald, S. M., Newville, M. Klingler, R. J., Winans, R. E., Almer, J. D. Sandi, G. and Srajer, G. (2012). Efficient simultaneous reverse Monte Carlo modeling of pair-distribution functions and extended x-ray-absorption fine structure spectra of crystalline disordered materials. J. Chem. Phys. 136, 074105-1-10.

[77] Triana, C. A., Araujo, C. M., Ahuja, R., Niklasson, G. A. and Edvinsson, T. (2016). Electronic transitions induced by short-range structural order in amorphous TiO_2. Phys. Rev. B. 94, 165129-1-9.

[78] Triana, C. A., Araujo, C. M., Ahuja, R., Niklasson, G. A. and Edvinsson, T. (2017). Disentangling the intricate atomic short-range order and electronic properties in amorphous transition metal oxides. Scientific Reports. 7, 1-12.

[79] Bunau, O., and Joly, Y. (2009). Self-consistent aspects of x-ray absorption calculations. J. Phys.: Condens. Matter. 21, 345501-1-11.

GRAPHICAL ABSTRACT

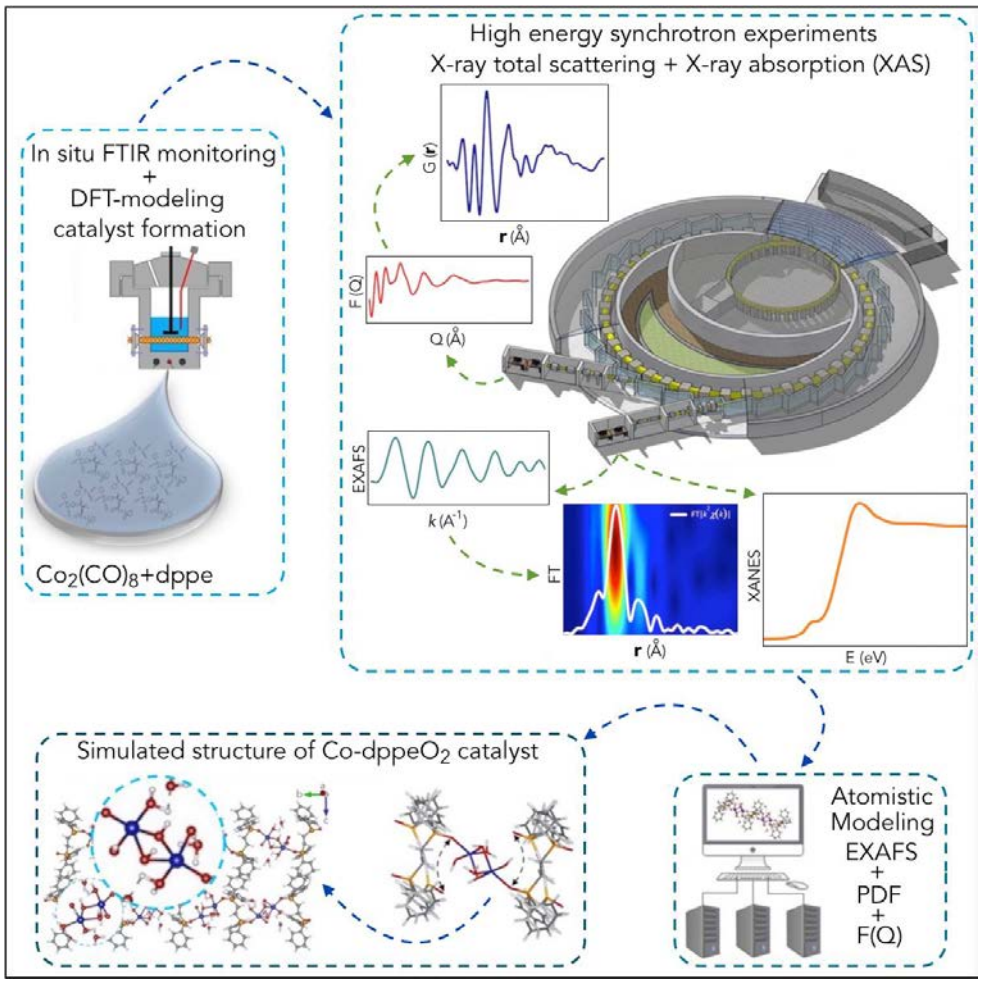

eToc Blurb

Designing hybrid organic-inorganic catalysts with bioinspired principles inspires applied catalyst development. We monitor the formation in situ and unravel the structure of a high-performance disordered hybrid cobalt oxidation catalyst. Atomistic modeling of X-ray scattering and absorption spectra identifies the catalyst as an unconventional cobalt coordination polymer of hydrated $\{H_2OCo_2(OH)_2\text{-}OH_2\}$ edge site motifs connected by bridging hydrophobic bisphosphine oxide ligands. The flexibility of this structural topology opens up new roads for rational design of disordered catalysts beyond molecules and solids.

HIGHLIGHTS

Structure of a soft-templated disordered 1D cobalt coordination polymer catalyst

Discerning the active catalytic site for high performance in alkaline electrolysis

In situ monitoring of catalyst formation to track the synthetic structural evolution

Understanding hydrated $\{H_2OCo_2(OH)_2\text{-}OH_2\}$ motifs within a flexible organic matrix.

PROGRESS AND POTENTIAL

The growing need for multifunctional and low-cost catalysts to store renewable energy resources has triggered great interest in new design concepts embracing their dynamic, and often disordered, features. This stands in sharp contrast to the challenges to reveal their atomic-range order, where major effort is still required to fully understand disordered catalysts. To date, few studies have focused on the almost unlimited combinations of metal centers and soft templating ligands that can create disordered hybrid catalysts. Our innovative, two-pillar strategy based on in situ monitoring and modeling of cutting-edge analytical data pushes these boundaries and explores a new disordered one-dimensional cobalt coordination polymer catalyst that outperforms conventional materials. Our results show the potential of soft templating of active moieties with flexible ligand environments and outline much-needed strategies to understand the functionalities of disordered catalysts.

KEYWORDS

Electrocatalysts; Oxygen evolution reaction; Water oxidation; Energy materials; Soft templating; Hybrid materials; Coordination polymers; Cobalt catalysts; Phosphine oxides; X-ray absorption spectroscopy; Pair distribution function; Reverse Monte Carlo simulations

Supplemental Information

Soft Templating and Disorder in an Applied 1D Cobalt Coordination Polymer Electrocatalyst

C. A. Triana, René Moré, Aaron J. Bloomfield, Predrag V. Petrović, Sara Goberna Ferrón, George Stanley, Snežana D. Zarić, Thomas Fox, Edward N. Brothers, Stafford W. Sheehan, Paul T. Anastas, and Greta R. Patzke

Supplemental Experimental Procedures and Supplemental Data

SUPPLEMENTAL EXPERIMENTAL PROCEDURES

Materials synthesis

$Co(dppe)Cl_2$ used as reference compound for the ^{31}P solid-state NMR measurements was obtained from Sigma-Aldrich and used without further purification. The synthesis of the solid-state NMR reference compounds $dppeO_2$ and $[Co(C_2H_5OH)_2(dppbO_2)_2(H_2O)_2](NO_3)_2 \cdot dppbO_2$ was carried out according to the protocol earlier described in refs. 1, 2.

$[Co(acac)_2(dppe)]BF_4$ was synthesized using a modified literature protocol.[3] $Co(acac)_3$ (0.361 g, 1.01 mmol), dppe (0.399 g, 1.00 mmol) and 58 mg activated charcoal were stirred in 30 mL EtOH/AcOH (10:1) for 24 h. The reaction mixture was filtered and the filtrate was diluted with 10 mL MeOH and 10 mL of KCl solution (20 mM). 425 mg of $NaBF_4$ was added. The solution was concentrated by rotavap until a precipitate was formed. The precipitate was dissolved in a minimum amount of MeOH:water (5:1) and kept for crystallization by slow evaporation. Crystallization afforded the product as red needles (yield: 544 mg, 0.73 mmol, 73 %).

^1H NMR (200 MHz, $CDCl_3$) 8.04 (m, arom.), 7.59 (m, arom.), 7.37 (m, arom.), 7.19 (m, arom.), 4.866 (s), 3.495 (m, CH_2), 3.116 (m, CH_2), 2.018 (s, $-CH_3$), 1.363 (s, $-CH_3$); ^{31}P NMR (81 MHz, $CDCl_3$) δ 48.454; FT-IR (ATR) υ = 3540, 3060, 2987, 2921, 1581, 1566, 1516, 1435, 1369, 1340, 1278, 1190, 1163, 1024, 868, 818, 779, 752, 718, 706, 689, 656, 636, 612, 533, 523, 481, 455, 431, 419 cm^{-1}; HRMS (ESI) m/z 655.15662 ($M-BF_4$), calc. for $[Co(acac)_2(dppe)]^+$ 655.157734.

In situ FTIR spectroscopy: SpectraTech High Pressure IR Cell

This design by SpectraTech (no longer in operation) and Parr Instrument Co. is based on a cylindrical attenuated total reflection (ATR) cell originally designed by William R. Moser.[4] A schematic for the cell is shown below in Figure M1 along with a photograph of the cell in a Bruker Tensor 27 FT-IR instrument showing the nitrogen-flushed PVC pipe additions to the cell holder that produces much better signal-to-noise when working with lower concentration samples.

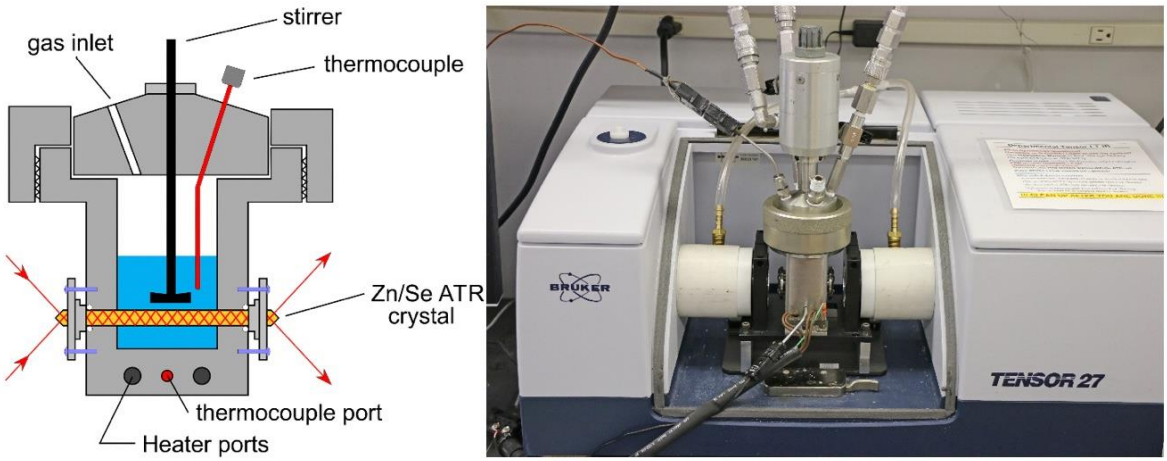

Figure M1. *Left*: schematic of the SpectraTech Circle ATR reaction cell. Teflon o-rings seal against the ZnSe cylindrical single-crystal rod and the autoclave to maintain a pressure seal. *Right*: photo of the cell in a Bruker Tensor 27 FT-IR instrument showing the PVC pipe additions to the cell holder that allows effective nitrogen purging along the IR path to and from the cell. The nitrogen purging significantly reduces water and CO_2 background and improves the overall signal-to-noise for experiments with lower concentration samples. The motorized stirrer assembly is not shown.

The cell is equipped with a motor-driven high-torque magnetic stirring system, electronic pressure transducer, thermocouple, rupture disk, gas inlet, and outlet ports. There is a small manifold next to the FT-IR with a regulator, 150 mL stainless steel reservoir equipped with another electronic pressure transducer, nitrogen line, and a quick-connect to which a one liter stainless steel tank with gasses of interest can be attached. The cell is rated to 1500 psig and 150 °C, although the maximum pressure we feel safe using is 300 psig. The refractive index for the silicon or ZnSe crystal rods changes with increasing temperature and combined with the long path length (5.715 cm). This limits the upper temperature to about 130 °C for Si or ZnSe.

Due to the temperature dependent refractive index changes, it is best to run the solvent as the background at various temperatures and utilize the appropriate solvent/temperature background for automatic subtraction when running the sample spectra at the same temperature. This was done for the mesitylene solvent used in the reaction study, and the negative peak at 1607 cm^{-1} is due to the subtracted mesitylene solvent background in the result spectrum.

A Parr 4850 process controller was used to control the stirring rate, heating and temperature of the cell, as well as measuring the pressures from the autoclave and gas reservoir transducers. The internal cell thermocouple is the primary control for heating and temperature control. The block thermocouple is tracked, but not used to control the temperature of the cell. The total cell volume is 28 mL, with 5 mL of reaction solution needed to cover the crystal rod. The stirrer is right above the crystal rod so that for stirred reactions a volume of 10-15 mL is typically used. Strongly absorbing metal carbonyl complexes can be run with concentrations as low as 5 mM, but 10-20 mM sample concentrations are usually better.

Experimental procedure

Mesitylene (anhydrous, ≥98 %) was sparged for 14 h with dry nitrogen before being brought into a nitrogen-filled drybox, where solutions of dicobalt octacarbonyl (0.080 g, 234 μmol, in 8.0 mL mesitylene, 29 mM) and 1,2-bis(diphenylphosphino)ethane ("dppe," 0.064 g, 161 μmol, in 15.0 mL mesitylene, 11 mM) were prepared. One gas-tight syringe was charged with dicobalt octacarbonyl solution (4.5 mL, 131 μmol), and another gas-tight syringe was charged with dppe solution (9.5 mL, 105 μmol).

The dicobalt octacarbonyl solution (4.5 mL, 131 μmol) was introduced to the reaction cell in the Bruker Tensor 27 spectrometer, which had been purged with dry nitrogen. The nitrogen atmosphere was replaced with dry CO, and an initial IR spectrum taken. The cell was stirred at 250 rpm, and the dppe solution (9.5 mL, 105 μmol) was added quickly. The cell was pressurized to 53 psig with CO, and allowed to react at ambient temperature (24 °C) with spectra recorded every 2 min (t = 0.5 min, 2.5 min, 4.5 min, and 6.5 min).

The reaction was then heated to 41 °C. Once the temperature had stabilized (*ca.* 10) min, spectra were recorded every 6 min for 18 min (3 spectra), then the temperature was increased to 60 °C. Once the temperature had stabilized (*ca.* 10) min, spectra were recorded every 6 min for 18 min (3 spectra), then the temperature was increased to 80 °C. Once the temperature had stabilized (*ca.* 10) min, spectra were recorded every 6 min for 42 min (7 spectra), then the temperature was increased to 100 °C. Once the temperature had stabilized (*ca.* 20) min, spectra were recorded every 6 min for 54 min (9 spectra), then the temperature was increased to 120 °C. Once the temperature had stabilized (*ca.* 20) min, spectra were recorded every 6 min for 138 min (23 spectra), then the temperature was allowed to cool to ambient temperature.

Once the temperature had reached 27 °C, a final spectrum was taken before the CO atmosphere was replaced with O_2 (25 psig), and spectra were recorded every 6 min for 3 h (30 spectra). The material was then transferred from the reaction cell to a beaker along with mesitylene washes of the reaction cell (2 × 5 mL). The contents were allowed to oxidize under air at 24 °C for 70 hours before the reaction was purified according to published procedures.[1]

Analytical characterization

Thermoanalysis

Thermogravimetric analysis (TGA) and differential scanning calorimetry (DSC) of Co-dppeO_2 was conducted using a Netzsch Jupiter STA 449 F3 TGA in an inert argon gas atmosphere.

Solid state nuclear magnetic resonance (NMR)

The solid state ^{31}P and ^{13}C NMR measurements were performed using a Bruker AV3-500 spectrometer (500.25 MHz, ^{1}H frequency).

High resolution transmission electron microscopy (HRTEM)

HRTEM measurements were performed at the IBM Research Zurich TEM facility employing a JEOL JEM–ARM200F microscope operated at 200 kV.

X-ray photoelectron spectroscopy (XPS)

XPS measurements were conducted using a physical electronics quantum 2000 X-ray photoelectron spectrometer featuring monochromatic Al-K_a radiation, generated from an electron beam operated at 15 kV and 32.3 W. The energy scale of the instrument was calibrated using Au and Cu reference samples. The spectra were taken from powders mounted on sticky carbon pads, which were then mounted onto a sample holder and introduced into the spectrometer. Analysis was conducted at 1×10^{-6} Pa, with an electron take off angle of 45° and a pass energy of 23.50 eV. Charge compensation in measurements was achieved using a low-energy electron source. To account for sample charging and to make the spectra comparable to each other, the binding energies of all spectra were aligned to C 1s at 284.8 eV.

SUPLEMENTAL DATA

In situ FTIR spectra for the oxidation time course and purified product FTIR spectra of Co-dppeO$_2$

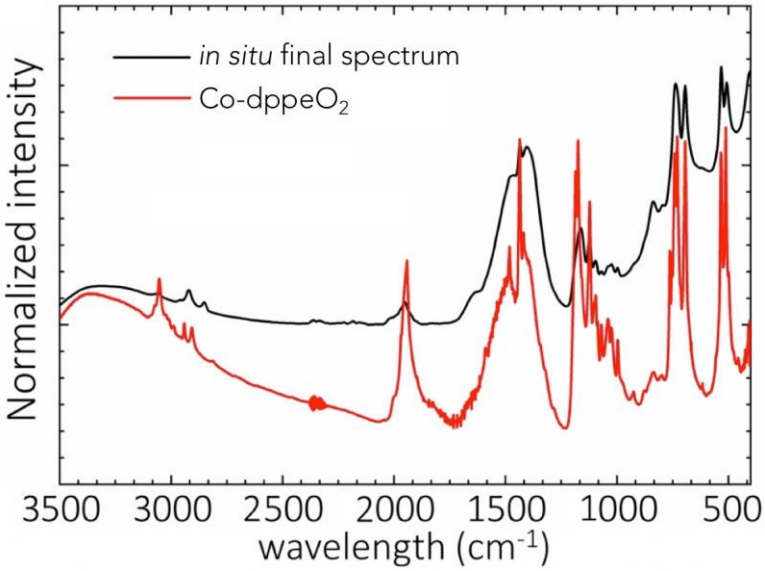

Figure S1. Final *in situ* FTIR spectrum *vs* the purified Co-dppeO$_2$ product.

Vibrational frequency calculations

As DFT calculations neglect the anharmonicity of the real system, and due to the basis set incompleteness and density functional limitations, the calculated vibrational modes will differ from the experimentally obtained vibrations. Thus, it is necessary to scale the calculated vibrations. The scaling factor was obtained by calculating the vibrational frequencies for the two isomers of dicobalt octacarbonyl (**Co1**, **Co2**) and cobalt tetracarbonyl anion (**A1**) in mesitylene (see Figure S2) using ωB97XD density functional, def2SVP basis set and two solvation methods (SMD and PCM). Calculated frequencies were then compared with the vibrations obtained experimentally for the dicobalt octacarbonyl in mesitylene (see Table S1). The scaling factor for each experimental vibration was divided by the respective calculated vibration, and the final scaling factor is the average value for all compared vibrations. The scaling factor resulting from the PCM solvation model was slightly closer to the factor of 1.0 and was thus used throughout this study. All the spectra for the candidate molecules were scaled by the factor of 0.9394. Figure S2 shows the comparison of the simulated spectra for the **A1**, **Co1** and **Co2** species after the scaling with the FTIR spectra of dicobalt octacarbonyl in mesitylene.

Table S1. Vibrations calculated for the two isomers of dicobalt octacarbonyl and cobalt tetracarbonyl anion using ωB97XD/def2svp with two solvation models (SMD and PCM) in mesitylene, vibrations from FTIR measurements for dicobalt octacarbonyl and calculated scaling factors.

Molecule	Calc. gas	Calc. mesitylene (SMD)	Calc. mesitylene (PCM)	Experimental mesitylene	Scaling factor (SMD)	Scaling factor (PCM)
Co1	2215	2208	2204	2077	0.9407	0.9424
	2194	2185	2180	2040	0.9336	0.9358
		2182	2178			
	2013	2004	1995			
	1996	1982	1974	1857	0.9369	0.9407
Co2	2212	2206	2201	2077	0.9415	0.9437
	2173	2159	2154	2025	0.9379	0.9401
A1	2031		2016	1883		0.9340
				Final scaling factor	0.9381	0.9394

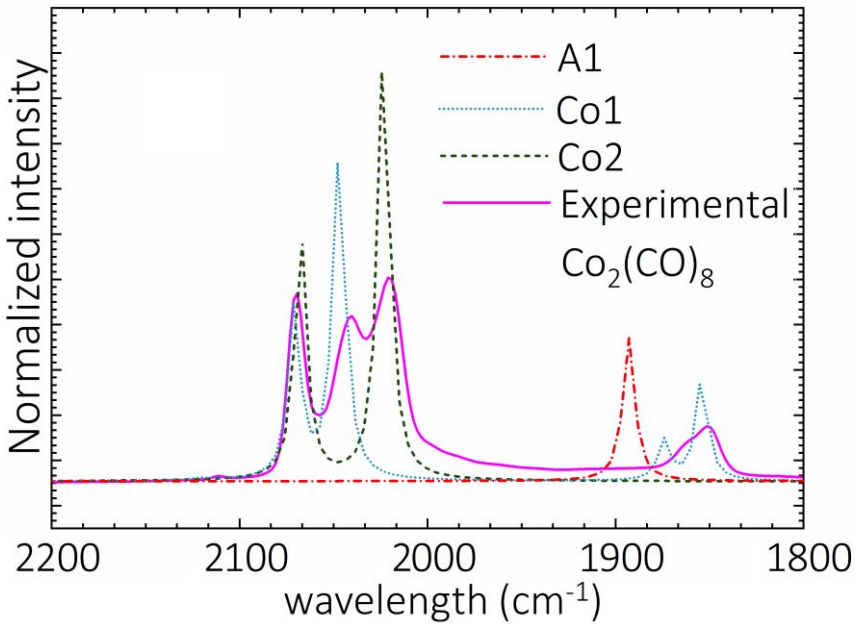

Figure S2. Simulated IR spectra for the two calculated isomers of $Co_2(CO)_8$ and $[Co(CO)_4]^-$ after the application of 0.9394 scaling factor *vs* experimental FTIR spectra of $Co_2(CO)_8$ in mesitylene. Modeled structures of **A1**, **Co1** and **Co2** were optimized with ωB97XD/def2svp level of theory in mesitylene.

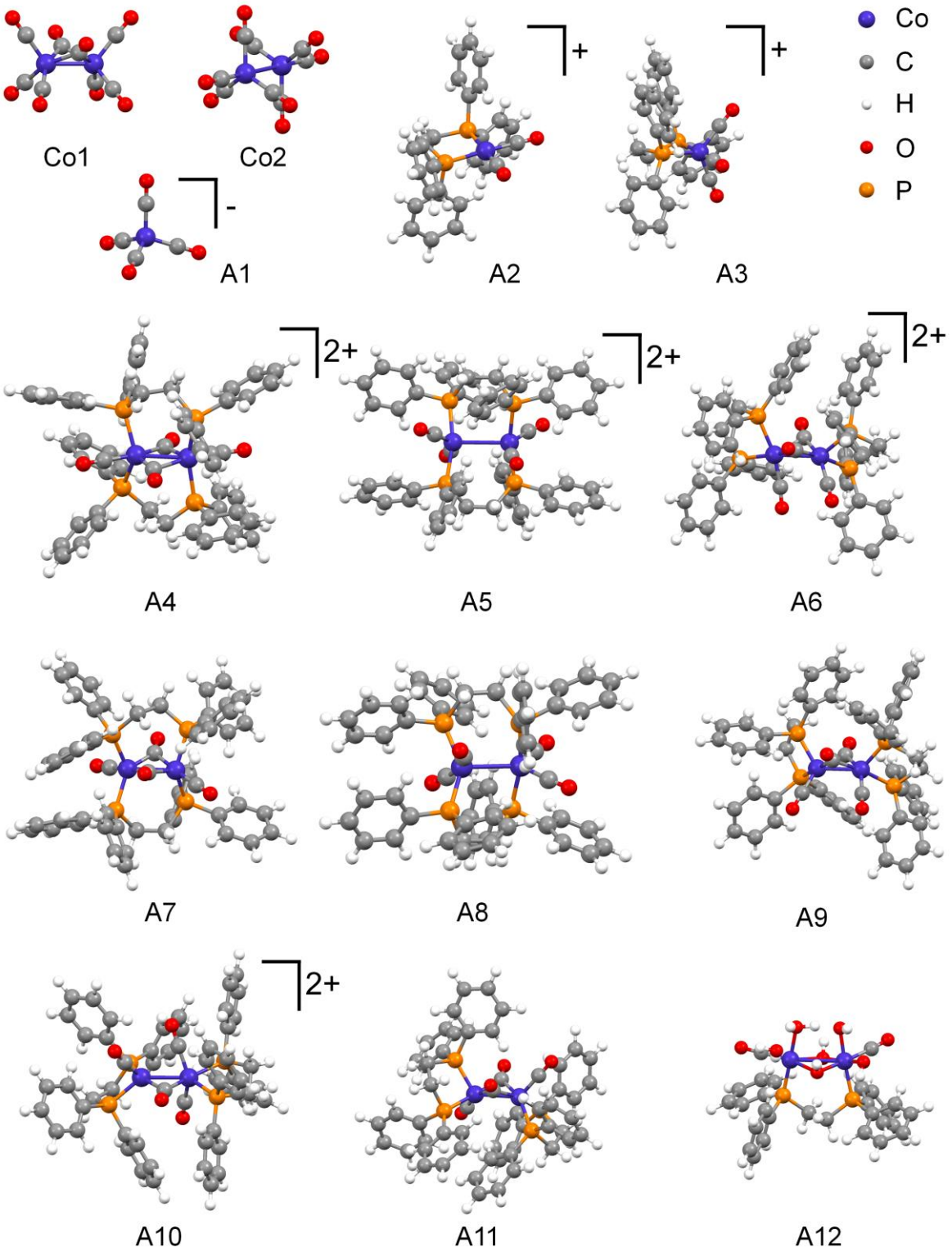

Figure S3. ωB97XD/def2svp optimized geometries in mesitylene for $Co_2(CO)_8$ isomers and Co-CO-dppe intermediate candidates (atom labels: inset at the top, right).

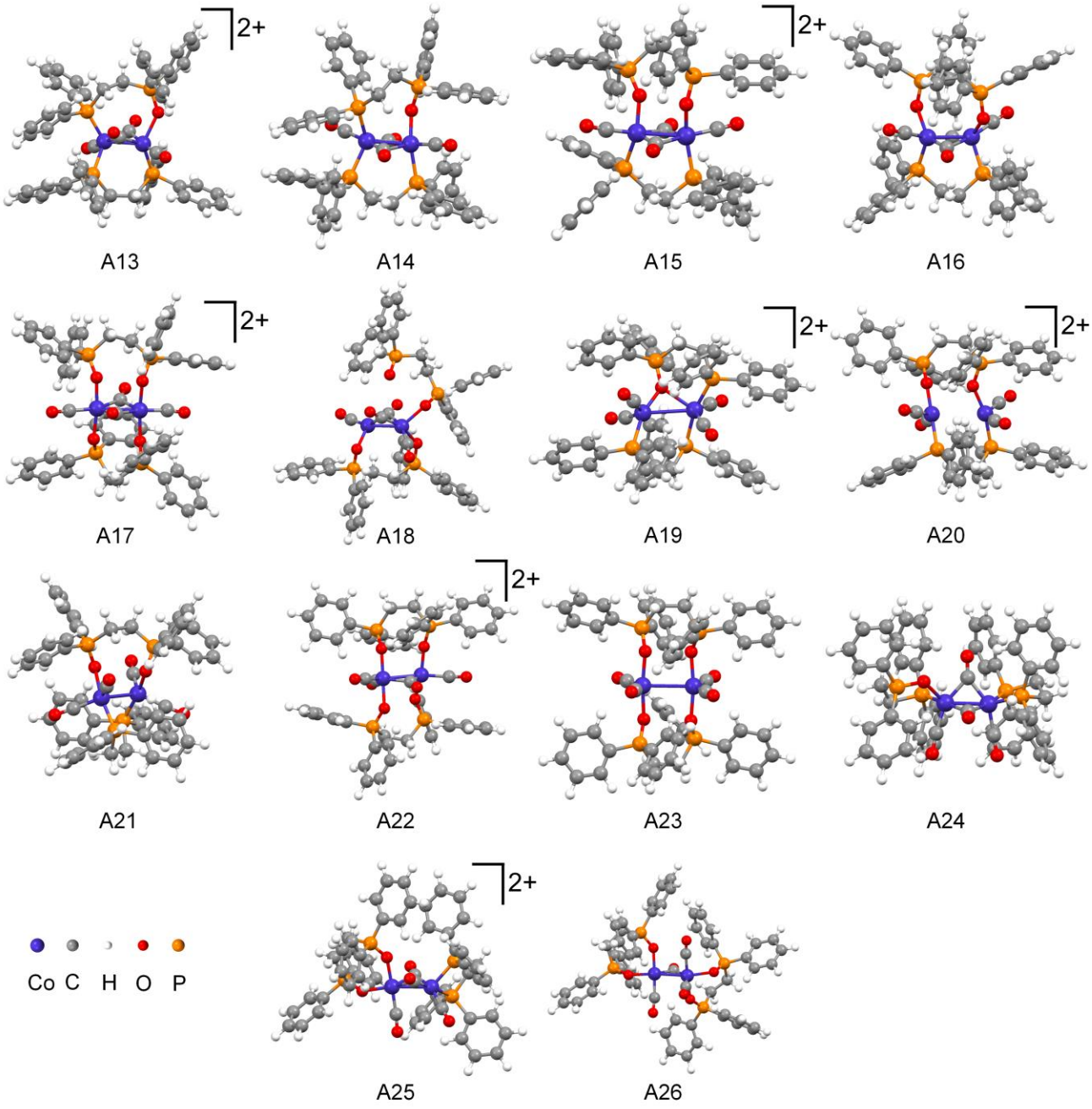

Figure S4 (continued from Figure S3): ωB97XD/def2svp optimized geometries in mesitylene for Co-CO-dppe intermediate candidates (atom labels: inset at the bottom, left).

The general formulae for the Co-CO-dppe intermediate candidate molecules shown in Figures **S3**, **S4** are given in Table S2.

Table S2. General formulae for the Co-CO-dppe intermediate candidates.

Compound	General formula		
A1	$[Co(CO)_4]^-$	A14	$[Co_2(\mu\text{-dppe})(\mu\text{-dppeO})(\mu\text{-CO})_2(CO)_2]$
A2	$[Co(dppe)(CO)_2]^+$	A15	$[Co_2(\mu\text{-dppe})(\mu\text{-dppeO}_2)(\mu\text{-CO})_2(CO)_2]^{2+}$
A3	$[Co(dppe)(CO)_3]^+$	A16	$[Co_2(\mu\text{-dppe})(\mu\text{-dppeO}_2)(\mu\text{-CO})_2(CO)_2]$
A4	$[Co(\mu\text{-dppe})(\mu\text{-CO})(CO)]_2^{2+}$	A17	$[Co(\mu\text{-dppeO}_2)(CO)(CO)]_2^{2+}$
A5	$[Co(\mu\text{-dppe})(CO)_2]_2^{2+}$	A18	$[Co(\mu\text{-dppeO}_2)(CO)(CO)]_2$
A6	$[Co(dppe)(\mu\text{-CO})(CO)]_2^{2+}$	A19	$[Co_2(\mu\text{-dppe})(\mu\text{-dppeO})(CO)_4]^{2+}$
A7	$[Co(\mu\text{-dppe})(\mu\text{-CO})(CO)]_2$	A20	$[Co_2(\mu\text{-dppe})(\mu\text{-dppeO}_2)(CO)_4]^{2+}$
A8	$[Co(\mu\text{-dppe})(CO)_2]_2$	A21	$[Co_2(\mu\text{-dppe})(\mu\text{-dppeO}_2)(CO)_4]$
A9	$[Co(dppe)(\mu\text{-CO})(CO)]_2$	A22	$[Co(\mu\text{-dppeO}_2)(CO)_2]_2^{2+}$
A10	$[Co_2(dppe)_2(\mu\text{-CO})(CO)_3]^{2+}$	A23	$[Co(\mu\text{-dppeO}_2)(CO)_2]_2$
A11	$[Co(dppe)(\mu\text{-CO})(CO)]_2$	A24	$[Co_2(dppe)(dppeO)(\mu\text{-CO})_2(CO)_2]$
A12	$[Co(\mu\text{-dppe})(CO)(H_2O)(\mu\text{-OH})(OH)]_2$	A25	$[Co_2(dppe)(dppeO_2)(\mu\text{-CO})_2(CO)_2]^{2+}$
A13	$[Co_2(\mu\text{-dppe})(\mu\text{-dppeO})(\mu\text{-CO})_2(CO)_2]^{2+}$	A26	$[Co(dppeO_2)(\mu\text{-CO})(CO)]_2^{2+}$

Table S3 show the vibrations of model complexes **A1**-**A12** in comparison to the *in situ* Co-CO-dppe at the beginning of the reaction with possible assignment of the terminal and bridging CO modes (asymmetric and symmetric stretching vibrations), while Table S4 lists significant peaks of model complexes **A13**-**A26** compared with the *in situ* spectra of the material after oxidation.

Table S3. Calculated and *in situ* IR vibrations at the beginning of the reaction for a selected region of the spectra (2200-1700 cm^{-1}). IR spectra were calculated with ωB97XD/def2svp level of theory in mesitylene.

A1	A2	A3	A4	A5	A6	A7	A8	A9	A10	A11	A12	Experimental 24 °C	Possible assignment[a]
-	2082(g)[b]	2096(s)	2085(g)	-	2085(g)	-	-	-	-	-	2246(n)	2085	term. CO str. sym.
-	-	2055(n)	2067(s)	2056(n)	-	-	-	-	2071(g)	-	2130(n)	2071	
-	2037(g)	2038(g)	-	-	2039(g)	-	-	-	-	-	-	2038	term. CO str. asym.
-	-	-	-	-	-	-	-	-	-	-	-	2019	
-	-	-	-	2006, 1996 (g)	-	-	-	1992(s)	-	-	-	2003	
-	-	-	-	-	-	1979(g)	-	-	-	1985(s)	-	1979	
-	-	-	1937(n)	-	-	1960(s)	1953(s)	1953(g)	1966(n)	1953(g)	1951(g)	1955	term. CO
1893(g)	-	-	1874(g)	-	1906, 1880 (g)	1775(n), 1710(n)	1913(s), 1984(s)	1775(n), 1696(n)	1861(g)	1775(n), 1710(n)	-	1920-1805 (br.)[c]	term. CO; brdg. str. sym.&asym.

[a] possible assignment of the vibration, term: terminal, brdg: bridging, str: stretching, sym: symmetric, asym: assymetric
[b] agreement with respective experimental vibration; g – good, s – somewhat, n – none.
[c] br: broad

Table S4. Calculated and *in situ* IR vibrations at the beginning of oxidation for a selected region of the spectra (2200-1700 cm^{-1}). IR spectra were calculated with ωB97XD/def2svp level of theory in mesitylene.

A13	A14	A15	A16	A17	A18	A19	A20	A21	A22	A23	A24	A25	A26	Exp.O_2 5 min
2104(n)[a]	-	2091(n)	-	-	-	-	-	-	2085(n)	-	-	2091(n)	2110(n)	-
-	-	2071(s)	-	-	-	-	2084(n)		2071(s)	-	-	-	2078(s)	2075(sh.)[b]
2064(g)	-	-	-	2064(g)	-	-	2064(g)	-	-	-	-	2058(s)	-	2063
-	-	-	-		-	2058(s)	-	-		-		-	-	2053(sh.)
-	-	-	-	-	-	2038(g)	-	-	-	-	-	-	-	2038(sh.)
-	-	-	-	-	-	-	2018(s)		2025(s)	-	-	-	-	2021
-	-	-	-	-	-	1999(g)	-	-	-	-	-	-		2001(sh.)
	1972(s)	-	1972(s)	-	-	1972(s)	-		-	-	1978(s)	-	-	1988(br.)
1946(s)	1946(s)	-	-	1959(g)	1959(g)	-	-	1953(s)	-	-	-	1940(n)	-	1959(sh.)
-	-	1920(s)	1939(n)	1920(s)	-	-	-	-	1920(s)	-	1920(s)	1927(g)		1926(sh.)
-	-	-	-	-	1990(g)	-	-	1900(g)	-	-	-	-	-	1899(sh.)[c]
-	-	1881(g)	-	-	-	-	-	1861(g)	-	-		-	1881(g)	1886(br.)
1868(s)	1769(n), 1729(n)	-	1742(n), 1703(n)	-	1874(g), 1749(n)	-	-	-	-	1874(g), 1835(n)	1769(n), 1729(n)	-	-	1871(sh.)

[a] agreement with respective experimental vibration; g – good, s – somewhat, n – none
[b] sh: shoulder, br: broad

X-ray photoelectron spectroscopy (XPS)

The XPS C 1s spectra do not show the presence of carbonates in Co-dppeO_2. The broad peak at ≈284.8 eV suggests a wider variety of chemical states (C-C, C-H, C-P) (Figure S5a). The peak at ≈531.6 eV in the O 1s spectrum indicates the chemical state of oxygen in Co-dppeO_2 involving OH groups. In CoO and Co_3O_4 as reference oxides, the O 1s spectra show an extra peak at ≈529.7 eV assigned to lattice oxygen (Figure S5b). The P 2p spectrum of Co-dppeO_2 arises from contributions due to P-O and P-C bonding as present in triphenylphosphine oxide (Figure S5c).

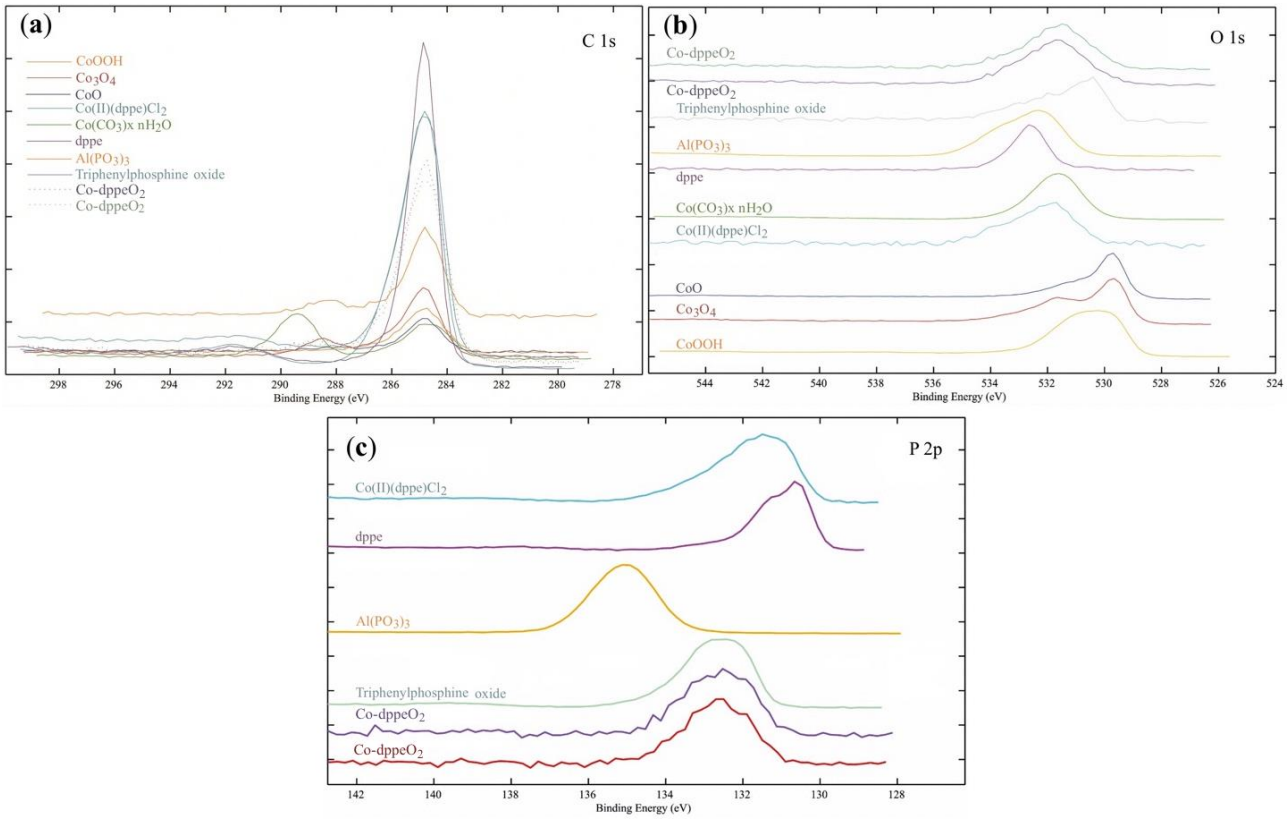

Figure S5. (**a**) C 1s, (**b**) O 1s and (**c**) P 2p XPS spectra of cobalt-containing reference oxides vs. those corresponding to Co-dppeO_2.

Solid-state ^{31}P and ^{13}C NMR spectroscopy

^{31}P-CP-MAS spectra of different reference compounds were recorded to allow a reasonable assignment for the spectrum of Co-dppeO_2. First, the ^{31}P NMR spectrum of commercial Co(dppe)Cl_2 shows a broad signal in the range between 15 and 80 ppm (Figure S6a). In this compound the phosphorus atoms of the dppe ligand are directly bound to the paramagnetic cobalt center which causes the expected paramagnetic line broadening. In contrast, a significantly less broadened signal was found for the diamagnetic complex [Co(acac)$_2$(dppe)]BF_4 (Figure S6b). In this case the ^{31}P resonance is mostly influenced by the quadrupolar properties of cobalt (^{59}Co, I=7/2) which leads to an octet-like lineshape around 47 ppm (half linewidth 3.4 kHz).[5] Free oxidized dppe (dppeO_2) shows three sharp ^{31}P lines (150-200 Hz broad) between 28 and 35 ppm, whereas free dppe causes one well-defined ^{31}P singlet (150 Hz) at -13.2 ppm (Figures S6c, S6d). The three signal components of the oxidized form of dppe (dppeO_2, Figure S6c) are obviously due to a distorted structure with more than one phosphorus site.[6] [Co(C_2H_5OH)$_2$(dppbO_2)$_2$(H_2O)$_2$](NO_3)$_2$·dppbO_2, the last reference compound with two oxidized phosphine ligands being coordinated via oxygen to the cobalt center and a third one embedded into the hydrogen bonding network,[2] exhibits one unresolved ^{31}P resonance (2.2 kHz broad) at 43.9 ppm (Figure S6e).

On the basis of these reference NMR experiments, the two ^{31}P signals of CodppeO_2 at 33.4 and 34.9 ppm (Figure S6f) can be attributed to two distinguishable phosphorus sites of dppeO_2 which is coordinated via its oxygen atoms to the cobalt centers. The chemical shift and the lineshape of the broad low-field component between 60-76 ppm seems to be related to those in Figure S6a, suggesting the presence of small residues of non-oxidized dppe which is directly bound via phosphorus to cobalt. Although, hence, such non-oxidized dppe ligands cannot be ruled out, we did not involve them in the model-motif since their contribution is just small and the spatial distribution unknown. In addition, the interatomic distances of those non-oxidized units will most probably overlap with those of the most dominant {Co_2(μ-OH)$_2$(OH)$_2$(H_2O)$_2$} units with dppeO_2 ligands.

The ^{13}C-CPMAS spectrum (Figure S6g) is not affected by paramagnetic influences, as it shows three separated resonances for the phenyl groups with typical aromatic shifts (128.8, 131.9 and 134.2 ppm) and inconspicuous linewidths (< 200 Hz). The two weak signals at 22.6 and 24.9 ppm are assigned to the CH groups of the phosphine ligand and do not show any paramagnetic line broadening either. Furthermore, the low number of aromatic resonances is an evidence for the spatial distortion of the phenyl groups due to residual mobility at these terminal positions.

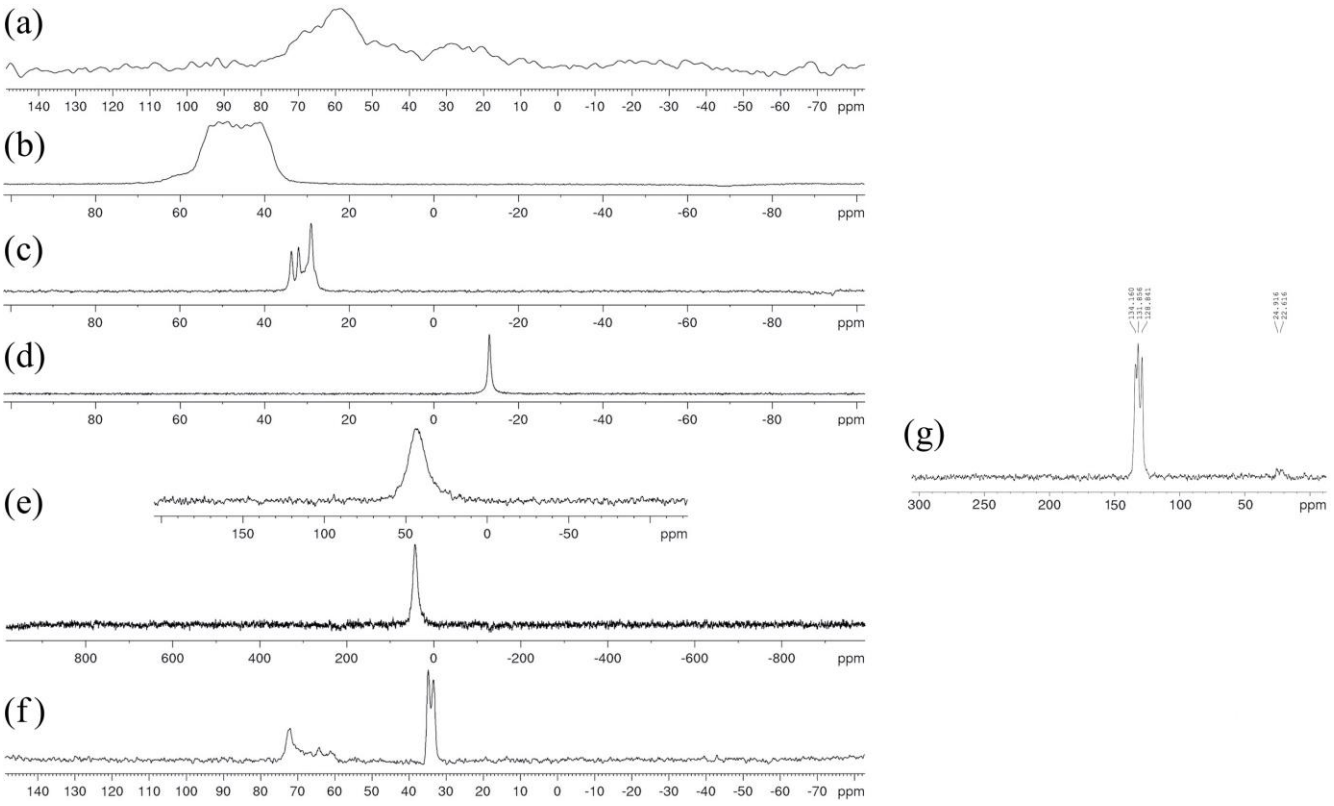

Figure S6. ^{31}P solid-state NMR spectra of reference compounds; (**a**) $Co(dppe)Cl_2$, (**b**) $[Co(acac)_2(dppe)]BF_4$, (**c**) $dppeO_2$, (**d**) dppe, (**e**) $[Co(C_2H_5OH)_2(dppbO_2)_2(H_2O)_2](NO_3)_2 \cdot dppbO_2$, (**f**) Co-$dppeO_2$, and (**g**) the ^{13}C NMR spectrum of Co-$dppeO_2$.

Thermal analysis and elemental analysis (TGA)

Thermogravimetric analysis of $CodppeO_2$ shows five weight loss steps (Figure S7). The first and second step (95 °C, 6.1 % and 240 °C, 11.16 %) are endothermic and can be attributed to the loss of water. The other three weight loss steps at 384 °C, 550 °C and 700 °C are all exothermic and can be assigned to the decomposition of the $dppeO_2$ ligand (Table S5). Additionally, Karl-Fischer titration showed a water content of 15 w-%, which fits well with the TGA results.

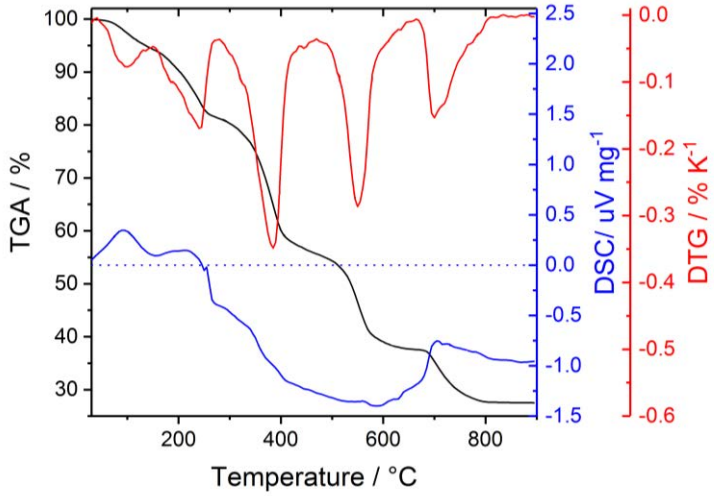

Figure S7. TGA/DTG and DSC analysis of Co-$dppeO_2$ (heating range 10 K/min in argon).

Table S5. Composition of Co-dppeO_2 and results from thermal analysis.

Composition (w%)		**Thermal analysis** T / °C	Δmass/ %	**assignment**
H_2O	15	95	6.10	endothermic, H_2O loss
C	45	240	11.16	endothermic, H_2O loss
H	4	384	23.59	exothermic, dppeO_2 decomposition
H/C ratio	1.06	550	18.87	exothermic, dppeO_2 decomposition
		700	12.84	exothermic, dppeO_2 decomposition
C/P=13.5 and C/H=0.7 vs. dppe: C/P=13 and C/H=11; Co:P = 1:1				
Co-dppeO_2 is comprised of 8.710 % P; 16.797 % Co (1:0.987 P/Co molar ratio)				

Calculated main interatomic distances from RMC modeling

Main interatomic distances obtained from RMC modeling of the $F(\boldsymbol{Q})$ and $G(\mathbf{r})$ spectra of Co-dppeO_2 are given in Table S6 below.

Table S6. Main interatomic distances of Co-dppeO_2.

Atom-Pairs	**Distance** (±0.03 Å)
C-H	0.96
C-C	1.42
Co-O	2.04
Co-H	2.21
Co-Co	2.92
Co-P	3.20
O-P	1.62

Simulated vibrational properties of Co-dppeO_2

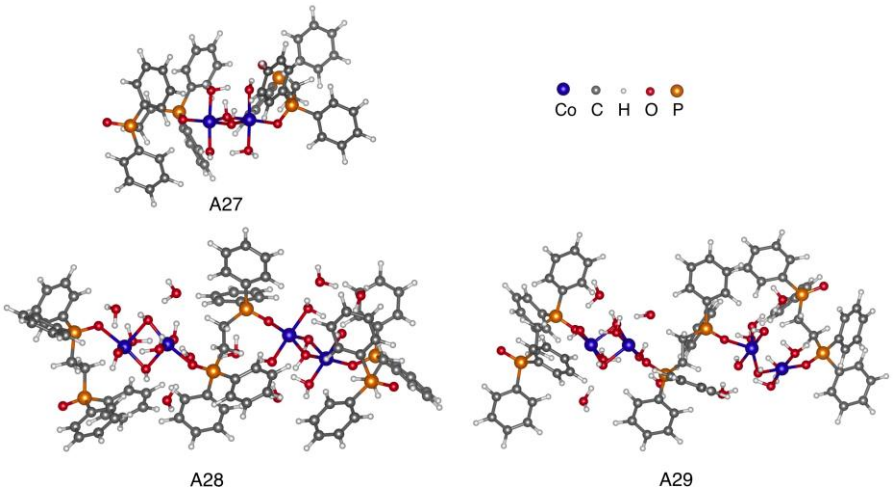

Figure S8. ωB97XD/def2svp optimized geometries in mesitylene of Co-dppeO_2 generated *de novo* **A27** and using the RMC-derived model-structural-motifs **A28** and **A29** (atom labels: inset at the top, right).

Table S7 shows selected vibrational modes for model complexes **A27**, **A28** and **A29** compared to the experimental spectra of the final purified Co-dppeO$_2$ complex. Possible assignments for the vibrational modes are also given, however, these should be considered very conservatively, since these vibrations overlap with (very) abundant C-C, C-H, and O-H stretching/bending modes due to the lack of environment influence, resulting in higher flexibility of the dppeO$_2$ ligands.

Table S7. Calculated vibrations from model complexes **A27**, **A28** and **A29** *vs* FTIR vibrations of the final Co-dppeO$_2$ product for a selected spectral region (1300-500 cm^{-1}). IR spectra were calculated with ωB97XD/def2svp level of theory in mesitylene.

A27	A28	A29	Final experimental	Assignment[a]
1929(s)[b]	-	-	1940(br.)[c]	O-H··O
1157(n)	1168(s), 1165(s)	1163(s)	1175	P-O str.
1129(s), 1118(s), 1112(n)	1116(s)	1147(n), 1136(s), 1115(s)	1123	P-O str.
1069(g), 1065(s), 1061(s)	1072(g), 1070(g), 1064(s)	1069(g), 1058(s)	1070	P-O str.
1037(s)	1048(s), 1046(s)	1043(g), 1038(g)	1040	P-O str.
543(g)	539(s)	540(s)	545(sh.)	Co-O(P) str.
535(g), 531(g)	532(g)	533(g)	533	Co-O str.
517(s), 514(g), 508(s)	511(g)	519(s), 513(g)	512	Co-O str.
500(g)	496(s)	499(g)	499(sh.)	Co-O str.

[a] possible assignment of the vibration, str: stretching
[b] agreement with respective experimental vibration; g – good, s – somewhat, n – none
[c] sh: shoulder, br: broad

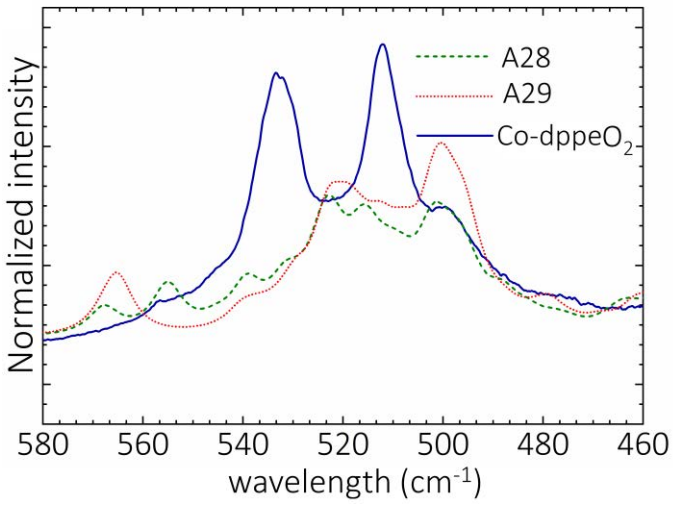

Figure S9. IR spectra calculated with ωB97XD/def2svp level of theory in mesitylene (Co-O bond vibration) for **A28** (green) and **A29** (red) structures compared with the FTIR spectra of Co-dppeO$_2$.

Ex situ FTIR and Raman spectra

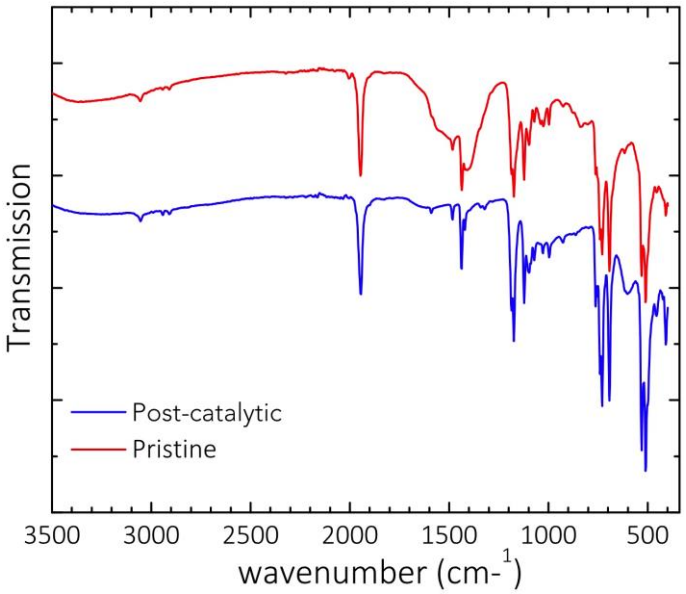

Figure S10. *Ex situ* IR spectra of Co-dppeO_2 before and after photocatalytic water oxidation both displaying a broad feature at ≈1950 cm^{-1} which could be assigned to a symmetrical hydrogen bond between a cobalt-bound water molecule (H-donor) and a hydroxide ion bound to the neighboring cobalt center (H-acceptor).

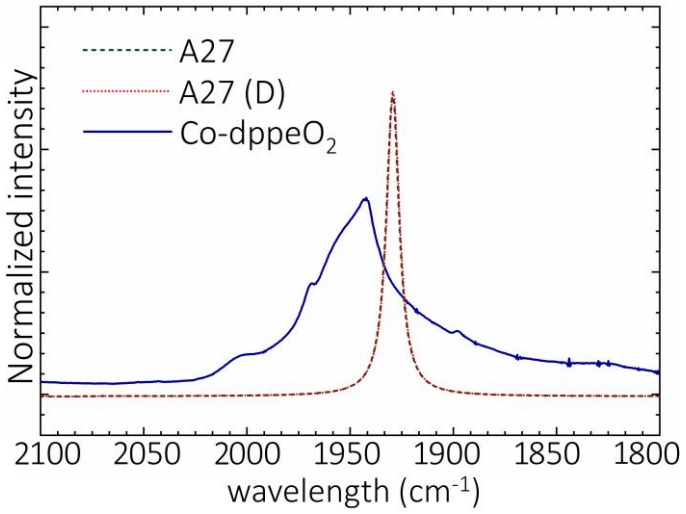

Figure S11. IR spectra calculated with ωB97XD/def2svp level of theory in mesitylene (O–H/D•••O bond vibration) for **A27** (green) and deuterated **A27** (red) structures compared with the FTIR spectrum of Co-dppeO_2.

Table S8. *Ex situ* FTIR and Raman vibrational modes of Co-dppeO_2.

IR	Raman	Assignment*
3057	3059	C-H str.
2943	2932	CH_2 asym. str.
2911	2902	CH_2 sym. str.
1947	——	Terminal CO str.
1590	1590	C=C ring str.
1483	——	C-H def.+semicircle str.
1436	——	C-H def.+semicircle str.
1185	1188	I.P. C-H def.
1175	1169	P-O str.
——	1111	Ring breath.
1040	——	I.P. C-H Def.
1024	1031	I.P. C-H Def.
997	1001	Trigonal ring breath.
693	692	Co-O Str.
530	——	O.P. Quadrant ring def.

*Str: Stretch; Def: Deformation; Asym: Asymmetric; I.P: In-plane; Sym: Symmetric.

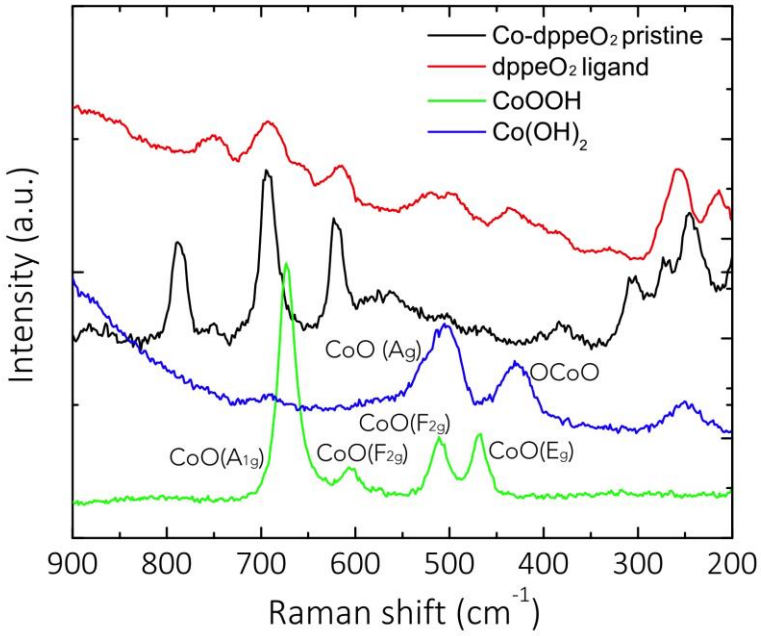

Figure S12. Comparison of the Raman spectra of Co-dppeO_2 with those of reference compounds dppeO_2, CoOOH and $Co(OH)_2$.

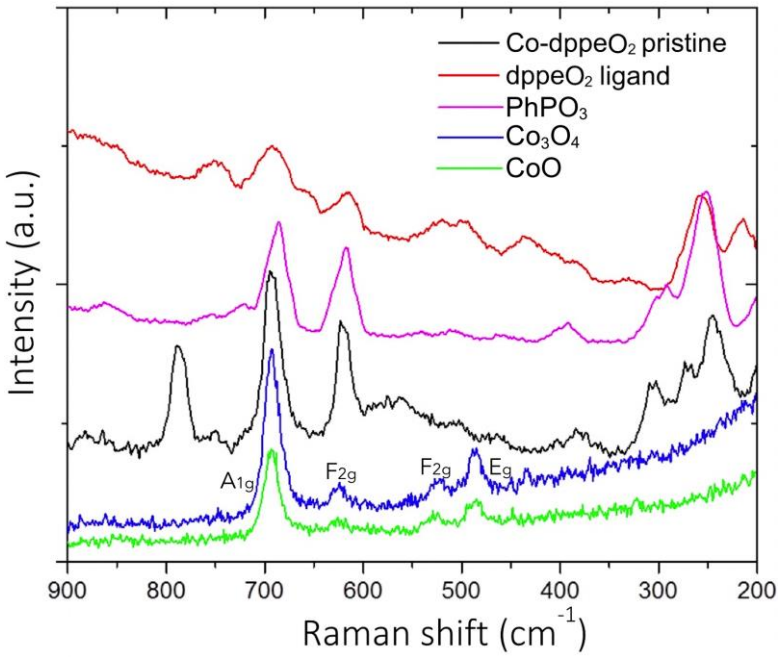

Figure S13. Comparison of the Raman spectra of Co-dppeO_2 with those of reference compounds dppeO_2, Ph_3PO, CoO and Co_3O_4.

High resolution transmission electron microscopy (HRTEM)

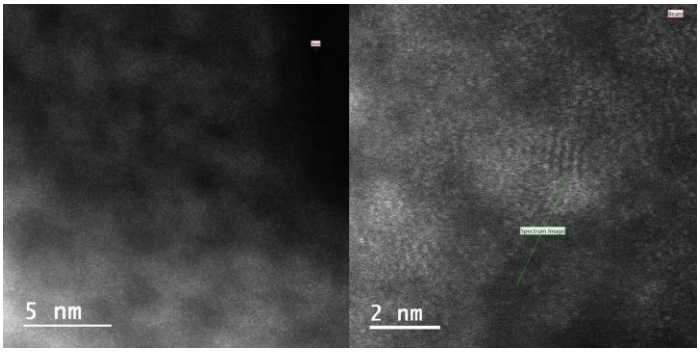

Figure S14. HRTEM images showing a disordered microstructure without traces of cobalt oxide particles.

References

1. Elson, K.E., Jenkins, I.D. and Loughlin, W.A. (2004). Cyclic analogues of Hendrickson 'POP' reagent. Aust. J. Chem. 57, 371-376.

2. Lees, A.M.J. and Platt A.W.G. (2009). Manganese(II) and cobalt(II) complexes of 1,4-bis(diphenylphosphinoyl)butane. Acta Cryst. C. 65, m10-m13.

3. Katoh, K., Sugiura, H., Kashiwabara, K. and Fujita J. (1984). Steric and Electronic Effects of Unidentate Tertiary Phosphine Ligands on Chemical and Absorption Spectral Properties of Their Mixed Cobalt(III) Complexes with Acetylacetonate Ions. Bull. Chem. Soc. Jpn. 57, 3580-3586.

4. Dardas, Z., Suer, M.G., Ma, Y.H., and Moser, W.R. (1996). High-Temperature, High-Pressure in Situ Reaction Monitoring of Heterogeneous Catalytic Processes under Supercritical Conditions by CIR-FTIR. J. Catal. 159, 204-211.

5. Asaro, F., Gobetto, R., Liguori, L., and Pellizer, G. (2009). Solution ^{31}P and ^{59}Co and solid-state ^{31}P CP/MAS NMR studies of triphenylphosphinecobaloximes. Chem. Phys. Lett. 300, 414-420.

6. Calcagno, P. Kariuki, B.M., Kitchin, S. J., Robinson, J.M.A., Philp, D., and Harris, K.D.M. (2000). Understanding the Structural Properties of a Homologous Series of Bis-diphenylphosphine Oxides. Chem. Eur. J. 6, 2338-2349.